

Neutrino-driven Explosions

Hans-Thomas Janka

Abstract The question why and how core-collapse supernovae (SNe) explode is one of the central and most long-standing riddles of stellar astrophysics. Solving this problem is crucial for deciphering the SN phenomenon, for predicting its observable signals such as light curves and spectra, nucleosynthesis yields, neutrinos, and gravitational waves, for defining the role of SNe in the dynamical and chemo-dynamical evolution of galaxies, and for explaining the birth conditions and properties of neutron stars (NSs) and stellar-mass black holes. Since the formation of such compact remnants releases over hundred times more energy in neutrinos than the kinetic energy of the SN explosion, neutrinos can be the decisive agents for powering the SN outburst. According to the standard paradigm of the neutrino-driven mechanism, the energy transfer by the intense neutrino flux to the medium behind the stagnating core-bounce shock, assisted by violent hydrodynamic mass motions (sometimes subsumed by the term “turbulence”), revives the outward shock motion and thus initiates the SN explosion. Because of the weak coupling of neutrinos in the region of this energy deposition, detailed, multi-dimensional hydrodynamic models including neutrino transport and a wide variety of physics are needed to assess the viability of the mechanism. Owing to advanced numerical codes and increasing supercomputer power, considerable progress has been achieved in our understanding of the physical processes that have to act in concert for the success of neutrino-driven explosions. First studies begin to reveal observational implications and avenues to test the theoretical picture by data from individual SNe and SN remnants but also from population-integrated observables. While models will be further refined, a real breakthrough is expected through the next Galactic core-collapse SN, when neutrinos and gravitational waves can be used to probe the conditions deep inside the dying star.

Hans-Thomas Janka
Max Planck Institute for Astrophysics, Karl-Schwarzschild-Str. 1, 85748 Garching, Germany
e-mail: thj@mpa-garching.mpg.de

1 Introduction

The term supernovae (SNe) was used for the first time in 1934 in three seminal papers by Baade and Zwicky (1934a,b,c), where the authors envisioned that “the super-nova process might occur to every star once in its lifetime, marking perhaps the cessation of its existence as an ordinary star.” Moreover, they hypothesized that these extremely luminous and energetic outbursts might signal the “transition of an ordinary star to a neutron star (NS), consisting mainly of neutrons.” Baade and Zwicky came forward with this truly visionary proposal at a time when the detailed nuclear processes in stars were not yet known. They based their arguments on the insight that the observed SN phenomenon releases an energy equal to a considerable fraction of the star’s rest mass, and they suggested that this energy originates from the gravitational binding energy of a very compact star that “may possess a very small radius and an extremely high density”, which “may far exceed the ordinary nuclear packing fractions” (Baade and Zwicky, 1934a).

This basic picture developed by Baade and Zwicky is still the foundation of our present notion of stellar death and the birth of NSs. The existence of NSs as well as their association with SN remnants is meanwhile firmly established by many observations, and the detection of two dozen neutrinos from SN 1987A in the underground experiments of Kamiokande II (Hirata et al, 1987), Irvine-Michigan-Brookhaven (IMB; Bionta et al, 1987), and Baksan (Alexeyev et al, 1988) was a direct confirmation of the scenario of stellar core collapse and hot NS formation. In fact, the huge binding energy released during this process, amounting approximately to

$$E_b \sim E_g \approx \frac{3}{5} \frac{GM_{\text{ns}}^2}{R_{\text{ns}}} \approx 3.6 \times 10^{53} \left(\frac{M_{\text{ns}}}{1.5 M_{\odot}} \right)^2 \left(\frac{R_{\text{ns}}}{10 \text{ km}} \right)^{-1} \text{ erg} \quad (1)$$

(M_{ns} is the NS mass and R_{ns} the NS radius in this Newtonian estimate for a homogeneous sphere), is mostly radiated in an intense pulse of neutrinos and antineutrinos, of which a few electron antineutrinos could be captured in the laboratories on earth. Less than one percent of the gravitational energy was sufficient to power the observed stellar explosion.

Initial Idea: Energy Arguments Because neutrinos carry away 100 times more energy than the kinetic energy of typical core-collapse SNe, these elementary particles were proposed by Colgate and White (1966) and Arnett (1966, 1967) as possible agents to drive the SN explosion. Although being trapped in the supra-nuclear interior of the newly formed NS for several seconds on average, neutrinos interact only by the weak force and therefore are able to leak out much faster than photons, whose electromagnetic reaction cross sections with matter are roughly 20 orders of magnitude larger. It is this property that allows neutrinos to transport energy out from deeper regions inside the hot NS on relevant time scales and to transfer some of this energy to the gravitationally more loosely bound surrounding layers. If this energy deposition is strong enough, the infalling matter of the stellar core can be lifted out of the gravitational trough of the NS to be expelled in the SN blast.

A Long and Winding Road of Learning It took more than 20 years of gradual improvements in the numerical treatments, new discoveries and insights on the microphysics side, and major revisions in many aspects of the early understanding of stellar core collapse, to advance the initially rather sketchy picture of the role of neutrinos in the SN explosion to a more consistent framework that is close to our modern view. On this way lay, for example, the introduction of multi-energy-group neutrino diffusion in the numerics sector; the discoveries of weak neutral currents and coherent scattering of neutrinos off nuclei; the recognition of the importance of an evolving, density and entropy dependent composition of heavy nuclei including their excited states, alpha particles, and free nucleons in nuclear statistical equilibrium during core collapse; the finding that neutrinos get trapped in the stellar plasma at a density of about $10^{12} \text{ g cm}^{-3}$ during infall, which renders the further evolution until core bounce essentially adiabatic; the insight that neutrino-electron scattering as well as electron captures on heavy nuclei besides free protons are important for determining the electron fraction Y_e (i.e., the electron-to-baryon ratio) and the entropy per baryon that the infalling matter carries into the trapping regime; and the understanding that the core collapse proceeds self-similarly with a homologous velocity profile ($v(r) \propto r$, r being the radius) in the subsonically contacting inner core, whose mass depends on the electron fraction ($M_{\text{ic}} \propto Y_e^2$) and determines the location at which the bounce-shock forms.

The space in this chapter is not sufficient to describe the theoretical arguments and evidence that have led to progress on these important aspects, whose evolution did not always follow a straight path and simple chronological order. The reader is referred to the excellent and exhaustive review by Bethe (1990) for the developments from the early steps of stellar core-collapse theory and explosion modeling in the mid 1960's until about 1990, and also to the later review by Janka et al (2007a), which attempts to report the new directions pursued afterwards and the corresponding updates of our knowledge.

The Delayed Neutrino-heating Mechanism With gradually improved numerical schemes and continuously increasing sophistication of the microphysics treatment used in core-collapse SN simulations, it became clear that the prompt bounce-shock mechanism, where the hydrodynamic shock front from the core bounce directly initiates the SN explosion, cannot succeed for the progenitor models provided by stellar evolution calculations. Instead of accelerating outward through the star, the shock experiences severe energy losses by nuclear photodisintegration of iron-group nuclei to free nucleons. Additional energy losses occur via a very short (~ 10 milliseconds) but extremely luminous flash of electron neutrinos at the moment when the shock breaks out of the neutrinosphere into the lower-density, outer regions of the iron core. As a consequence, the shock front stalls at only 100–200 km even before being able to reach the surface of the stellar iron core. Some extra source of energy must come to the aid of the stagnating shock.

At this point, as a revival of the idea that was born in the mid 1960's, neutrino energy transfer came back into play through simulations by Wilson (1985), which provided new hints to the possibility that neutrino heating could indeed lead to a

rejuvenation of the stalled shock, but at a much later stage after core bounce than expected. The scenario of the “delayed neutrino-heating mechanism” was born and was worked out conceptually and quantitatively in some detail in a paper by Bethe and Wilson (1985). Some hundred milliseconds after shock stagnation, the conditions between the newly formed NS and the stalled shock front become favorable for efficient neutrino-energy deposition, because the temperatures in this region decrease, while the NS heats up during its contraction and radiates neutrinos with increasingly harder spectra. If neutrinos are able to transfer enough energy to the postshock medium, the rise in pressure is able to accelerate the shock outwards against the ram pressure of the surrounding, still collapsing stellar shells. In this mechanism the shock expansion is driven by the neutrino-energy deposition (and not by momentum transfer!) to the stellar plasma. This is consistent with the fact that the neutrino luminosities radiated by the nascent NS stay considerably below the Eddington limit.

New Lessons from Supernova 1987A Wilson’s delayed neutrino-driven mechanism has become the paradigm for explaining the explosions of the majority of all core-collapse SNe, although his results depended on a number of uncertain assumptions and could not be reproduced by modern simulations with more refined numerical tools and state-of-the-art input physics. Moreover, SN 1987A has led to a major revision of the simple picture of spherically symmetric explosions, which Wilson and others (even much later) tried to establish with one-dimensional simulations (assuming that all physical variables depend only on the radius). SN 1987A, being the closest SN for hundreds of years and thus being observed with unprecedented detailedness, revealed the spectacle of a stellar death from the earliest moments of radiation emission on. Therefore, SN 1987A provided, for the first time, unambiguous evidence that strong hydrodynamic mixing processes played a role even already during the first second of the explosion, when radioactive elements such as ^{56}Ni (which provides the energy for the long-lasting high luminosity of a SN) are nucleosynthesized.

Indeed, the first multi-dimensional simulations, which could be carried out shortly later in two spatial dimensions (i.e. assuming, for simplicity, axisymmetry around an arbitrary direction; Herant et al, 1994; Burrows et al, 1995; Janka and Müller, 1994; Janka and Müller, 1995, 1996), demonstrated that violent convective overturn develops in the neutrino-heated postshock layer because of negative entropy gradients. These hydrodynamic instabilities lead to non-radial flows that may explain the observed asymmetries and radial mixing effects in SN 1987A. Furthermore, they can also provide crucial support to the neutrino-driven mechanism, potentially solving the dilemma that Wilson’s first successes could not be confirmed by later spherical models, in which the neutrino heating remained too weak to revive the stalled SN shock.

A Challenging Problem Until Today The unexpected scientific insight, triggered by SN 1987A, that SN explosions are generically non-spherical, still poses major challenges for today’s numerical modeling. It implies that three-dimensional (3D) simulations are needed to capture the true nature of the phenomenon of stellar core

collapse and explosion, and, in particular, of the physical mechanism that initiates the SN blast. For 20 years since the mid 1990's, SN computations have struggled with the enormous demands of multi-dimensional neutrino transport, and only very recently the first simulations have become possible in full three dimensions due to the growing supercomputer power and newly developed, massively parallel simulation codes.

The main algorithmic as well as computational challenges are connected to the neutrino propagation in the six-dimensional phase space (made up of three spatial and three momentum variables) and to the complexity of the neutrino-matter interactions, which require the coupling of neutrinos and antineutrinos over the whole phase space. Both aspects together turn neutrino transport into an integro-differential problem with high demands on numerical efficiency and computing capabilities. Even at the present time, all SN simulations therefore still use approximations in various aspects, and the solution of the crucial problem of neutrino transport in six-dimensional phase space and full generality will require supercomputing on the exascale level. Ultimately, this step will have to be taken, shall numerical models convincingly demonstrate the viability of the neutrino-heating mechanism and make quantitative predictions of its observational implications.

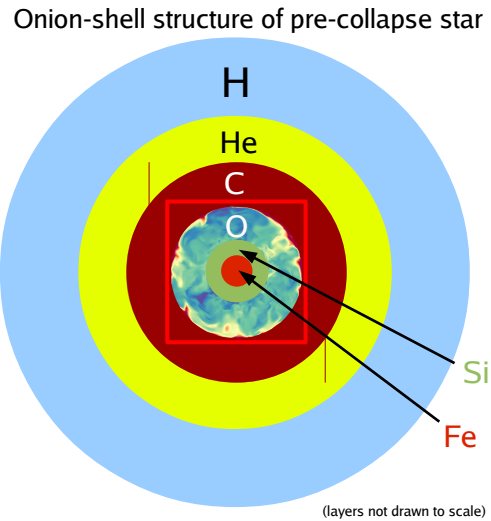
Lack of Convincing Alternatives Even today, after appreciable improvements on the modeling side and considerable progress in our understanding of the processes that play a role during stellar collapse and explosion, the neutrino-driven mechanism is not yet finally established as the solution of the SN problem. Success has been reported for stars near the low-mass end of the SN progenitors (i.e., stars between roughly $8 M_{\odot}$ and about $10 M_{\odot}$ with O-Ne-Mg or Fe cores), which develop neutrino-driven explosions quite readily. The predicted explosion properties such as energy, radioactive nickel yield, and intermediate-mass nucleosynthesis, seem to agree with those of the Crab SN and some extragalactic subluminescent SNe. For more massive progenitors, however, the situation is still ambiguous. Although modern 3D simulations could obtain explosions and thus provide support for the viability of the neutrino-heating mechanism in principle, the models are not yet able to demonstrate that the mechanism is robust and that it is able to explain SN explosions with the observed energies.

These results should be considered only as a preliminary step, because more work is needed to further improve the modeling. Interpretation of the remaining shortcomings and still open questions as fundamental weaknesses or even failure of the neutrino-driven mechanism is not justified in view of the extreme complexity of the problem and the enormous challenges to perform realistic simulations in all details. In this context it is also important to note that convincing alternatives based on well-justified assumptions concerning the relevant physics, do not exist. The most interesting alternative possibility are magnetohydrodynamic explosions, in which strong magnetic fields play a crucial role in pushing the SN shock. Magnetic fields that thread a rapidly spinning stellar core are amplified during collapse by compression, rotational winding, and the magnetorotational instability (e.g., Akiyama et al, 2003, and references therein), tapping the gravitational and rotational energy of the

newly formed NS. In the shear layer between the surface of the NS and the stalled SN shock, magnetic pressure can build up to accelerate the shock front and to launch magnetic jets along the rotation axis. This magnetorotational mechanism can work on relevant time scales only in stars with stellar cores that spin much more rapidly than in the far majority of SN progenitors, where angular momentum transport and loss through magnetic fields and stellar winds lead to efficient core deceleration during the evolution through the red-giant phase (Heger et al, 2005).

Connection to Observations Ultimately, observational evidence is needed to decipher the secrets of the explosion mechanism of core-collapse SNe for a final solution of this long-standing and nagging problem of stellar astrophysics. For this reason, SN modeling has to strive for explanations of observational phenomena and has to predict discriminating diagnostic effects. Before the next Galactic SN will offer the unique chance to perform high-precision measurements of neutrino and gravitational-wave signals as direct probes from the very center of a dying star, SN theory must confront its predictions with the huge wealth of data available from well studied individual SNe and SN remnants. Also the messages communicated by the entire population of such events and their relic objects should be exploited for constraints of the explosion physics. This Chapter will also review current efforts in this direction.

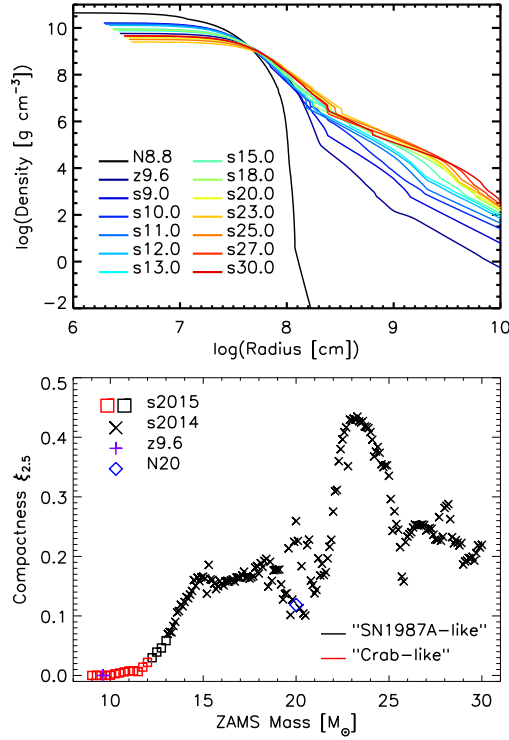
Fig. 1 Onion-shell structure of a SN progenitor star prior to the onset of stellar core collapse. Shells of progressively heavier elements contain the ashes of a sequence of nuclear burning stages, which finally build up a degenerate core of oxygen, neon and magnesium or iron-group elements at the center. Convective burning can lead to large-scale velocity and density perturbations in the oxygen and silicon layers (as indicated for the O-shell). The red box marks the volume that is zoomed into in Fig. 3



2 From Stellar Core Collapse to Explosion

Massive stars, when approaching the end of their hydrostatic evolution, develop the so-called onion-shell structure (Fig. 1), where shells of lighter chemical elements surround layers of successively heavier elements, which contain the ashes of a long sequence of nuclear burning stages starting with hydrogen burning on the main sequence of the color-magnitude diagram. At the end of the stellar life, the central core is composed of oxygen, neon and magnesium or of iron-group elements and is stabilized against gravity mainly by the pressure of degenerate electrons. Before its collapse sets in, the baryonic mass of such a degenerate core ranges between slightly less than $1.3 M_{\odot}$ and roughly $2 M_{\odot}$ with central densities between several 10^9 g cm^{-3} and more than $\sim 10^{10} \text{ g cm}^{-3}$, central temperatures around 10^{10} K (roughly 1 MeV in energy units), entropies per nucleon of typically about $1 k_B$, and electron-to-baryon ratios between ~ 0.45 and ~ 0.50 .

Fig. 2 Density profiles (*top*) and compactness values $\xi_{2.5}$ (Eq. 2 for $M = 2.5 M_{\odot}$; *bottom*) for selected progenitor stars with ZAMS masses between $8.8 M_{\odot}$ and $30 M_{\odot}$. N8.8 denotes an $8.8 M_{\odot}$ O-Ne-Mg-core progenitor from Nomoto (1984, 1987), N20 a $20 M_{\odot}$ SN 1987A progenitor from Nomoto and Hashimoto (1988), z9.6 a $9.6 M_{\odot}$ zero-metallicity progenitor provided by A. Heger (2012, private communication), and all s-models are solar metallicity progenitors from Sukhbold and Woosley (2014), Woosley and Heger (2015b), and Sukhbold et al (2016). The progenitors with the smallest compactness values are classified as ‘‘Crab-like’’, the more compact iron-core progenitors as ‘‘SN1987A-like’’. (Figures courtesy of Thomas Ertl)



2.1 Core Structure of Stars at Collapse

The density structure at the time of stellar core collapse exhibits considerable variability between different stars (Fig. 2, upper panel). When evolved to the same central density, however, the density profiles of the degenerate cores become nearly identical, simply because the conditions are still close to hydrostatic equilibrium and the equation-of-state is dominated by relativistic electrons, therefore is well described by a polytrope with adiabatic index of $4/3$. In contrast, the density profiles of the surrounding shells exhibit a wide spread of gradients, from abrupt “cliffs” bordering O-Ne-Mg cores in super-AGB stars, to steep slopes in progenitors with masses below about $10 M_{\odot}$, to much shallower declines in more massive stars (Fig. 2, upper panel).

In order to characterize these differences of the stellar density profiles, O’Connor and Ott (2011) introduced a “compactness” parameter,

$$\xi_M = \frac{M/M_{\odot}}{R(M)/(1000\text{km})}, \quad (2)$$

which is defined as the ratio of a chosen mass to the radius that encloses this mass. Figure 2 (lower panel) displays ξ_M for $M = 2.5 M_{\odot}$ as a function of the zero-age-main-sequence (ZAMS) mass for a state-of-the-art set of SN progenitors. Any other choice of M/M_{\odot} between ~ 1.5 and ~ 2.5 yields a similar pattern. The functional behavior is also independent of whether ξ_M is measured at the onset of the core collapse, at a moment when the collapsing stellar cores reach a certain central density, or at core bounce, despite some quantitative evolution taking place between these stages for the smaller values of M/M_{\odot} in the mentioned mass interval. The non-monotonic variations above a ZAMS mass of about $15 M_{\odot}$ are a consequence of a complex interplay of carbon and oxygen shell burning, which can cause large differences in the compactness for stars of very nearly the same mass (Sukhbold and Woosley, 2014).

Low-mass progenitors of less than roughly $12 M_{\odot}$ possess the lowest core-compactness values, whereas above $\sim 12 M_{\odot}$ the compactness, e.g. $\xi_{2.5}$, increases steeply (Fig. 2, lower panel). Observations and theoretical models suggest that the Crab Nebula is probably the remnant of a low-mass progenitor, most likely of a star with less than about $10 M_{\odot}$, which exploded with a very low energy ($\lesssim 10^{50}$ erg) and little ^{56}Ni production ($\lesssim 10^{-2} M_{\odot}$) (e.g., Nomoto et al, 1982; Kitaura et al, 2006; Yang and Chevalier, 2015; Owen and Barlow, 2015). Progenitors with a similarly small core compactness and with SN explosion energies and ^{56}Ni production below average are therefore denoted as “Crab-like” in Fig. 2, whereas stars more massive than $12 M_{\odot}$ are classified as “SN1987A-like”, because their explosion parameters are closer to those of SN 1987A as a more canonical iron-core SN. This distinction, however, is not strict. Considering a more rigorous constraint on the decline of the mass infall rate during stellar core collapse, for example, Müller (2016) delimits SN progenitors above $\sim 10 M_{\odot}$ from stars below this mass limit, whose extremely tenu-

ous envelope around the degenerate iron core defines a particularly close structural proximity to O-Ne-Mg-core progenitors.

The compactness of the layers surrounding the degenerate central core has important consequences for the way how neutrino-driven explosions develop. This will be discussed in a later section.

2.2 Evolution Phases of Neutrino-driven Explosions

The dynamical evolution from the onset of stellar core collapse to the successful initiation of the SN outburst can be divided into six stages, which are displayed in a graphical way in Fig. 3.

Gravitational Instability and Collapse of the Stellar Core The gravitational instability of the degenerate O-Ne-Mg or iron core (Fig. 3, top left) is initiated by electron captures on nuclei and free protons,

$$e^- + p \longrightarrow \nu_e + n, \quad (3)$$

$$e^- + (A, Z) \longrightarrow \nu_e + (A, Z - 1), \quad (4)$$

and by the partial photodissociation of heavy nuclei to α particles and free nucleons (for a discussion in detail, see Langanke et al, 2003; Hix et al, 2003; Janka et al, 2007b). Both lead to a reduction of the effective adiabatic index of the equation of state below the critical value for gravitational instability of about $4/3$. Initially, the electron neutrinos (ν_e) produced by electron captures can escape freely, but at a density of some $10^{11} \text{ g cm}^{-3}$, the neutrino mean free path for coherent neutrino scattering off heavy nuclei becomes so short that the neutrinos begin to diffuse. Finally, at a density of about $10^{12} \text{ g cm}^{-3}$, the outward neutrino diffusion is slower than the accelerating infall of the stellar plasma, and neutrino trapping sets in. With neutrinos being unable to escape, the entropy remains conserved, and the subsequent infall proceeds adiabatically. The subsonically collapsing inner core develops a homologous velocity profile, which reaches a maximum velocity near the interface to a nearly free-falling, supersonic outer core. (An excellent text-book discussion of the physics during this phase is provided by Shapiro and Teukolsky, 1983, Chapter 18.)

Core Bounce and Shock Formation The implosion of the inner core is stopped abruptly when nuclear saturation density ($\rho_0 \approx 2.7 \times 10^{14} \text{ g cm}^{-3}$ or $n_0 \approx 0.16 \text{ fm}^{-3}$) is reached at the center and the phase transition to homogeneous nuclear matter leads to a sudden stiffening of the equation of state. The increase of the adiabatic index above $4/3$ allows for a new stable state where the stellar matter can be supported against its own gravitational attraction by the internal pressure of the nucleon gas, which is highly incompressible due to the repulsive part of the nucleon-nucleon interaction potential. Since the collapsing inner core overshoots the new equilibrium state, it bounces back and its expansion creates pressure waves that steepen into a shock front at the transition to the supersonically infalling outer core (Fig. 3, top

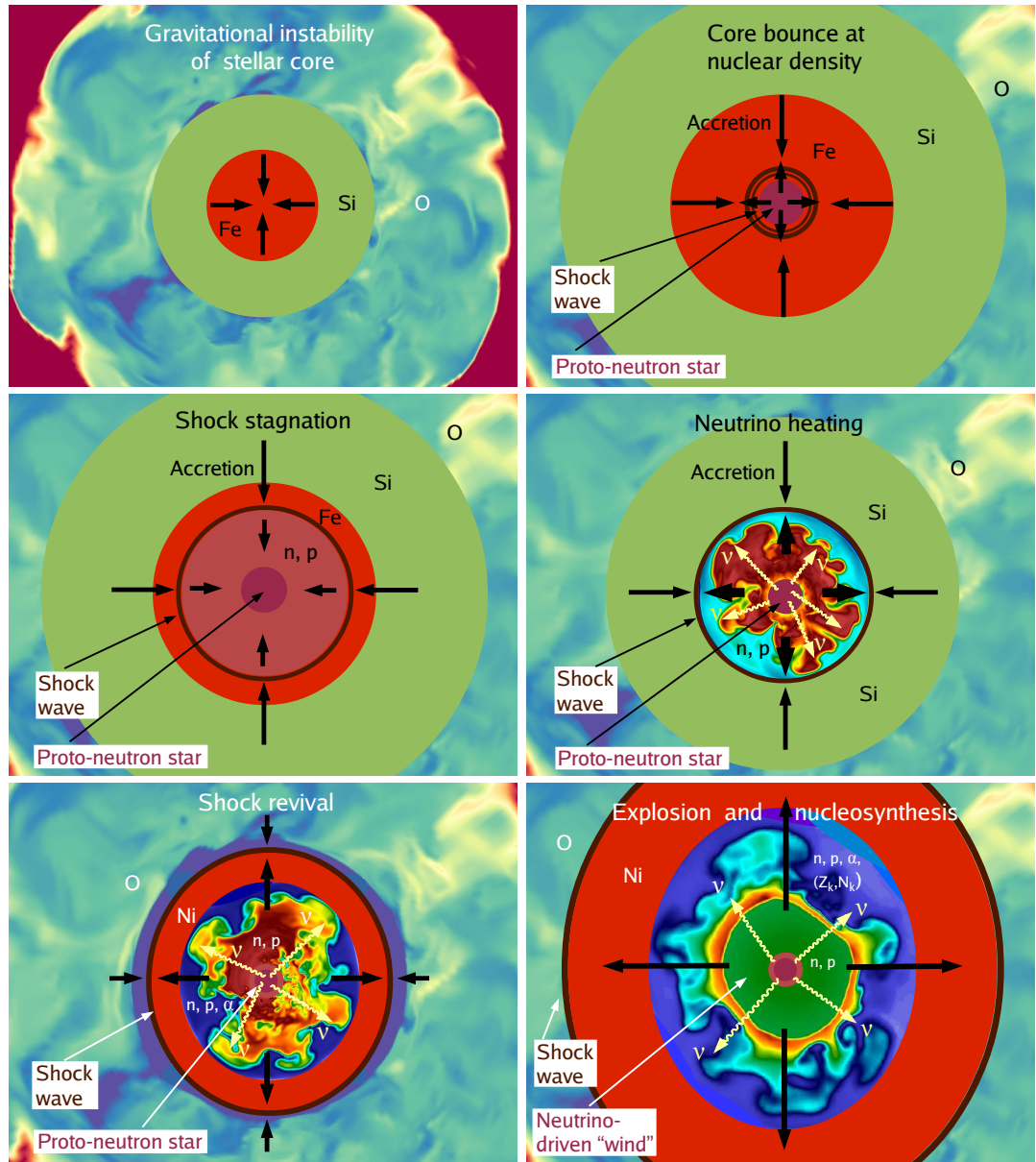


Fig. 3 Dynamical phases of stellar core collapse and explosion by the neutrino-driven mechanism: infall, core bounce, stagnation of the bounce shock, accretion and neutrino heating, shock revival, and outward acceleration of the neutrino-powered SN shock front (*from top left to bottom right*). The horizontal scales of the plots are roughly 15,000 km, 4000 km, 4000 km, 2000 km, 2000 km, and 10,000 km, respectively. The different shells are not displayed to scale, but the central regions and the new-born, hot NS (the “proto-NS”) are (approximately logarithmically) enlarged compared to the outer layers. Superimposed on the graphical elements are results from 3D simulations of pre-collapse convective O-shell burning by Müller et al (2016b) and of postshock asymmetries (buoyant plumes of high-entropy matter and accretion cooler downflows) during the first second of the SN explosion as computed by Wongwathanarat et al (2013). In the bottom-right image the spherical neutrino-driven wind, composed of free neutrons and protons (n, p), is visible in green. It recombines to α -particles and heavy nuclei (Z_k, N_k) when the temperatures decrease in the expanding outflow. The sharp, nearly spherical discontinuity bounding the green area is the reverse shock that terminates the supersonic expansion of the neutrino-driven wind

right). Because of the initial loss of electron neutrinos, the electron fraction at the center has dropped to values between 0.25 and 0.27, and the inner core has shrunk to a mass below $0.5 M_{\odot}$, which roughly defines the location where the bounce-shock forms, nearly independent of the progenitor star and only moderately different (within $\sim 10\%$) for different models of the nuclear equation of state (Janka et al, 2012).

Shock Stagnation and Shock-breakout Neutrino Burst The newly formed shock begins to propagate outwards in radius as well as in mass. Dissipation of kinetic energy in the infalling matter swept up by the shock raises the entropy and temperature within the shock, creating high-energy photons that lead to the photodissociation of iron nuclei to free nucleons. The iron disintegration is essentially complete as long as the shock radius is smaller than the “dissociation radius” of iron,

$$R_{\text{diss}} = \frac{GMm_{\text{u}}}{8.8\text{MeV}} \gtrsim 160 \left(\frac{M}{M_{\odot}} \right) \text{ km}, \quad (5)$$

which is roughly given by the radius where the nuclear binding energy of nucleons (with average mass m_{u}) in iron-group material equals the free-fall kinetic energy (with velocity v_{ff}) in the gravitational potential of the enclosed mass M : $\frac{1}{2}m_{\text{u}}v_{\text{ff}}^2 = GMm_{\text{u}}R_{\text{diss}}^{-1} = 8.8\text{MeV}$. The conversion of kinetic energy to rest-mass energy thus drains about 8.8 MeV per nucleon or 1.7×10^{51} erg per $0.1 M_{\odot}$ of energy from the thermal reservoir, reducing the postshock pressure. Within only about a millisecond and after having overrun only about $0.5 M_{\odot}$ of iron-core matter, the bounce shock comes to a stop still well inside of the collapsing iron core (Fig. 3, middle left). At about this time the density behind the shock has decreased to a value where the electron neutrinos, which are abundantly produced by electron captures onto free protons in the postshock medium (Eq. 3), start to escape freely. A luminous flash of ν_e , the so-called shock-breakout neutrino burst, is radiated and takes away additional energy from the postshock layer. Since the velocities everywhere behind the shock become negative, the shock expansion stalls and the shock converts into an accretion shock.

Neutrino Heating and Accretion Shortly after core bounce neutrino emission carries away energy from the postshock layer. The conditions, however, change fundamentally at later post-bounce times, because the postshock temperature decreases as the density drops and the plasma becomes more radiation dominated. Parallel to that, the neutrino spectra radiated from the contracting and increasingly hotter NS harden. While the first effect diminishes the neutrino cooling at the shock, the second effect allows for an increasing fraction of the electron neutrinos (ν_e) and antineutrinos ($\bar{\nu}_e$) streaming away from the neutrinosphere to be reabsorbed by free neutrons and protons,



closer to the shock front (Fig. 3, middle right). This situation defines the phase of neutrino heating, when the stalled shock receives fresh energy from the neutrinos streaming up from the neutrinosphere. Since neutrino-energy deposition creates a negative entropy gradient, the heated layer can become convectively unstable (Herant et al, 1994; Burrows et al, 1995; Janka and Müller, 1996; Foglizzo et al, 2006). Also the standing-accretion-shock instability (SASI; Blondin et al, 2003; Blondin and Mezzacappa, 2007; Scheck et al, 2008; Foglizzo et al, 2015) can grow in the mass-accretion flow between shock and nascent NS, leading to large-scale, non-radial deformation and violent sloshing and spiral motions of the shock front, thus stirring the whole layer enclosed by the shock and the NS. Mushroom-like high-entropy structures indicative of buoyancy-driven Rayleigh-Taylor instability can be seen in the postshock region in the middle-right panel of Fig. 3.

Shock Revival Neutrino-energy transfer to the shock raises the postshock pressure. If the heating by neutrinos is strong enough, the shock can be pushed outwards and the SN explosion can be launched. The non-radial fluid instabilities (buoyancy, convective overturn, and the SASI) assist the neutrino-heating mechanism in several ways. Besides causing more expansion of the shock and thus enlarging the layer of neutrino-energy deposition, the non-radial flows carry hot, neutrino-heated matter outwards to the shock and cooler gas inward, closer to the NS, where this material can absorb energy from the neutrino flux more effectively. In combination, the multi-dimensional effects increase the efficiency of the neutrino-energy transfer compared to the case of spherical conditions. If the thermal pressure behind the shock, supported by turbulent pressure, overcomes the ram pressure of the infalling preshock layer, runaway shock expansion can set in (e.g., Janka and Müller, 1996; Murphy and Burrows, 2008; Nordhaus et al, 2010; Hanke et al, 2012; Couch and O’Connor, 2014; Fernández et al, 2014; Fernández, 2015). The outward acceleration of the shock begins to trigger explosive nucleosynthesis in the postshock medium (Fig. 3, bottom left), producing also radioactive iron-group and intermediate-mass nuclei (e.g., $^{56,57}\text{Ni}$, $^{55,60}\text{Co}$, ^{44}Ti), which power the luminous, long-time electromagnetic radiation of the expanding SN debris for many years.

Explosion and Nucleosynthesis For a transient period of time, matter swept up by the accelerating SN shock is still accreted towards the nascent NS, absorbs energy from neutrinos, and is partly ejected outwards again. When this phase of simultaneous mass accretion and outflow (which might last for several seconds; Müller, 2015) ends, neutrino-energy deposition in the near-surface layers of the new-born NS launches the so-called neutrino-driven wind, which is an essentially spherical, tenuous outflow of baryonic matter from the NS surface (Fig. 3, bottom right). This high-entropy (several 10 to over $100 k_B$ per nucleon) medium is initially composed of free neutrons and protons, which recombine to α -particles and finally partly to heavy nuclei when the expanding outflow cools. Depending on whether there is neutron or proton excess in the outflow, neutron- or proton-rich nuclei may be assembled in the neutrino-driven wind and can add interesting nucleosynthetic yields to the innermost SN ejecta (for a review of possible processes, see Janka et al, 2007b; Janka, 2012). While the shock propagates outwards through the progenitor star (and

needs hours to over a day to reach the stellar surface), the compact remnant left behind at the center cools and deleptonizes by radiating neutrinos and antineutrinos of all flavors. With the decaying neutrino emission also the neutrino-driven wind gradually loses power and finally dies off.

2.3 State-of-the-art Multi-dimensional Models

Owing to the high performance of modern parallel computers and efficient application codes, self-consistent simulations of stellar core collapse with detailed neutrino transport have become possible in three spatial dimensions. These models begin to lend support to the viability of the neutrino-driven mechanism and thus confirm the promising perspectives that have been drawn by a growing number of successful explosions in two-dimensional (2D) simulations. The latter models, however, suffer from the enforced constraint of symmetry around a chosen axis. While this assumption reduces the computational complexity and costs considerably, the artificially imposed symmetry channels the flow along the preferred direction and also implies that turbulent energy cascades inversely to the 3D case (Hanke et al, 2012). Models in 2D could therefore only be a preliminary step before 3D simulations became feasible.

2.3.1 Electron-capture Supernovae and Low-mass Iron-core Explosions

Low-mass SN progenitors with O-Ne-Mg cores (super-AGB stars) or iron cores possess particularly steep density profiles and extremely small values of the core compactness (see Sect. 2.1). This characteristic pre-collapse property facilitates neutrino-driven explosions to develop fairly easily and early after core bounce. The reason is a very rapid decline of the mass-accretion rate,

$$\dot{M} \approx \frac{2M}{t_{\text{infall}}} \frac{\rho}{\bar{\rho}} = \frac{8\rho}{\sqrt{3}} \sqrt{GMr^3}, \quad (8)$$

as a consequence of a density decline $\rho(r)$ that is much steeper than $r^{-3/2}$ (t_{infall} is the collapse time scale of a stellar shell with density $\rho(r)$ at initial radius r , $\bar{\rho}$ the average density inside of r , and M the mass enclosed by r , which is essentially equal to the NS mass in the case of low-mass progenitors; Müller, 2016). This leads to a fast drop of the ram pressure of matter falling into the shock, for which reason the shock expands quickly and establishes favorable conditions for neutrino-energy deposition around the newly formed NS (Kitaura et al, 2006; Janka et al, 2008). The SN explosion is thus powered by a neutrino-driven wind absorbing energy from the neutrinos leaving the NS. Due to their extremely steep density profiles, some low-mass SN progenitors (such as those with O-Ne-Mg cores) are the only cases where explosions can be obtained even in spherically symmetric (1D) simulations. Never-

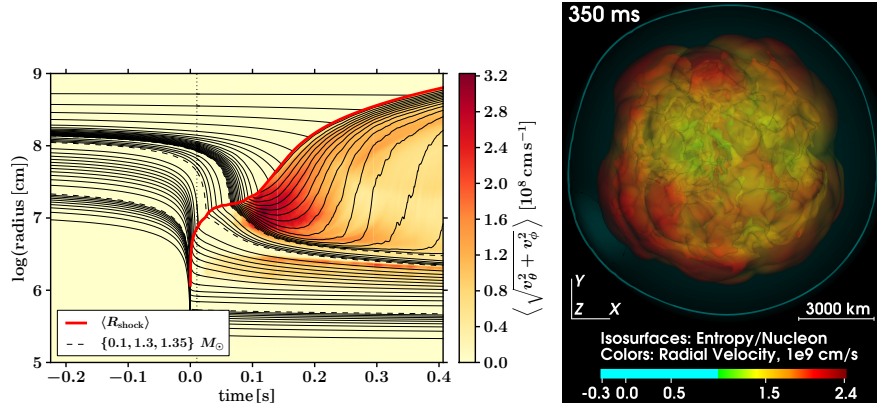


Fig. 4 Explosion of a $9.6 M_\odot$ progenitor by the neutrino-driven mechanism in a self-consistent 3D simulation (Melson et al, 2015b). *Left*: Time evolution displayed by a mass-shell plot showing radii versus time (normalized to core bounce) for selected values of the enclosed mass, with the dashed curves corresponding to three exemplary masses listed in the inset in the lower left corner. The thick red line starting at core bounce marks the trajectory of the SN shock. While the collapse of the stellar core is visible by contracting mass shells, converging shells in the lower part of the figure indicate the formation of the NS and outgoing shells signal the ejection of overlying matter in the SN explosion and the onset of a neutrino-driven wind from the surface of the new-born NS. The color coding depicts angular averages of the non-radial velocities with red hues indicating strong convective mass motions in the neutrino-heated region behind the SN shock. *Right*: Ray-tracing image of the beginning explosion (350 ms after core bounce). The SN shock is visible as a bluish, nearly circular line, enclosing convectively perturbed high-entropy bubbles of neutrino-heated matter (visualized by semi-transparent isosurfaces for chosen values of the plasma entropy per nucleon). The color coding indicates radial velocities with red corresponding to the highest values (see color bar). The shock has a diameter of about 12,000 km. (Figure from Melson et al, 2015b, © The American Astronomical Society)

theless, hydrodynamic instabilities develop in the neutrino-heated postshock layer and have important consequences for explosion asymmetries and the nucleosynthesis conditions in the innermost SN ejecta (Wanajo et al, 2011).

In the case of O-Ne-Mg-core progenitors the shock propagates outwards continuously and accelerates rapidly at about 50–70 ms after core bounce (Kitaura et al, 2006; Janka et al, 2008; Fischer et al, 2010). Neutrino-heated plasma rises buoyantly in Rayleigh-Taylor fingers, but the structures freeze out on relatively small angular scales because of their fast outward expansion. Also the $9.6 M_\odot$ iron-core progenitor of Fig. 2 explodes in 1D, though only later than ~ 300 ms after bounce. In this case convective overturn pushes the shock and speeds up the explosion considerably (Fig. 4), making it also more energetic (Melson et al, 2015b). In both cases, however, multi-dimensional simulations predict subenergetic SNe with explosion energies of $\sim (0.5\text{--}1.5) \times 10^{50}$ erg and fairly little production of radioactive nickel (several $10^{-3} M_\odot$), which is compatible with a growing sample of low-luminosity Type IIP SNe and which has also been inferred for SN 1054 as the birth event of the Crab Nebula (Yang and Chevalier, 2015).

Because of their similar explosion dynamics in terms of a rapid outward acceleration of the SN shock and a fast expansion of the postshock material, the nucleosynthesis in low-mass SNe is very similar, irrespective of the different nature of the progenitor stars with O-Ne-Mg or iron cores. This rapid expansion leads to ν_e and $\bar{\nu}_e$ absorption reactions (Eqs. 6, 7) and their inverse processes to quickly freeze out in the ejecta, enabling matter, in particular in the heads of the Rayleigh-Taylor mushrooms, to be expelled with considerable neutron excess. This facilitates the formation of neutron-rich nuclei. Low-mass SNe could thus not only produce interesting amounts of ^{48}Ca and ^{60}Fe but could also be dominant contributors to the Galactic repository of light trans-iron elements from zinc to zirconium, potentially even of light r-process nuclei up to palladium and silver (Wanajo et al, 2011, 2013a,b).

Explosions of progenitor stars with O-Ne-Mg cores are often called “electron-capture SNe”, because the collapse of the highly degenerate stellar core is mainly initiated by electron captures on magnesium and neon, in contrast to more massive progenitors with iron cores, where nuclear photodisintegration plays the dominant role. However, it is important to note that neither the explosion mechanism of these SNe nor their nucleosynthesis are distinct from those of low-mass progenitors with iron cores.

2.3.2 Supernovae of Massive Iron-core Progenitors

Explosions develop considerably less readily in progenitor stars more massive than, roughly, $10 M_\odot$. In particular, neutrino-driven explosions for such stars cannot be obtained in spherical symmetry, which means that the explosion mechanism is generically multi-dimensional. Non-radial hydrodynamic instabilities, i.e., buoyant Rayleigh-Taylor plumes, convective overturn, SASI mass motions, and turbulent flow fragmentation in the postshock layer play a crucial role for the success of the mechanism, instead of being just an accompanying phenomenon. They provide decisive support for the shock expansion and thus can foster explosions even when 1D simulations fail (see, e.g., Herant et al 1994; Burrows et al 1995; Janka and Müller 1996; Murphy and Burrows 2008; Nordhaus et al 2010; Hanke et al 2012, and for reviews Janka 2012; Burrows 2013; Janka et al 2016; Müller 2016).

The higher mass-accretion rate (\dot{M}) of the collapsing core of massive SN progenitors, which increases with higher values of the core compactness, has two competing effects. On the one hand a higher mass accretion rate hampers the outward expansion of the stalled SN shock, because it has to be overcome by the postshock pressure P_s :

$$P_s \geq (1 - \beta_\rho^{-1}) \rho_0 v_0^2 = \frac{\dot{M} \sqrt{2GM}}{4\pi R_s^{5/2}}, \quad (9)$$

where R_s is the shock-stagnation radius, and

$$v_0 \approx -\sqrt{\frac{2GM}{R_s}}, \quad (10)$$

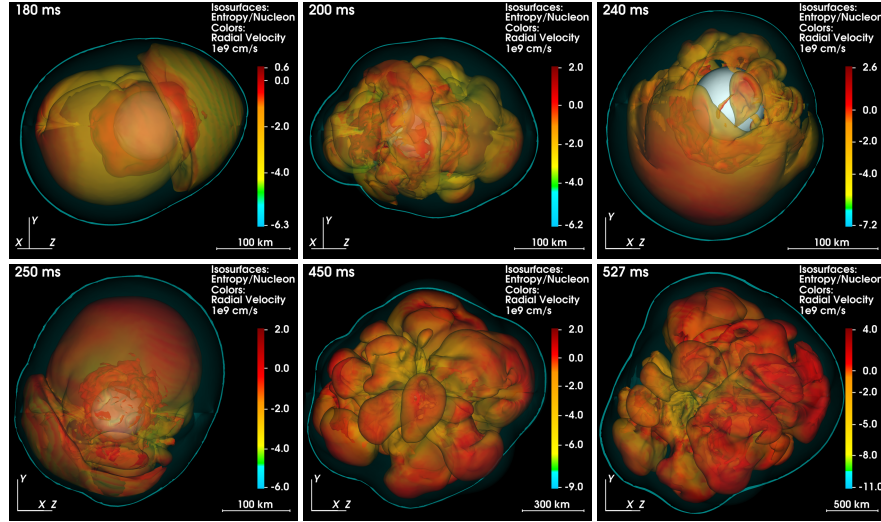


Fig. 5 Explosion of a $20 M_{\odot}$ progenitor by the neutrino-driven mechanism in a self-consistent 3D simulation (Melson et al, 2015a). The sequence of ray-tracing images (with post-bounce times given in the upper left corners) shows that the postshock layer is massively stirred by phases of violent sloshing and spiral motions due to the standing accretion shock instability (SASI), whose presence can be recognized by dominant dipolar and quadrupolar shock-deformation modes. Run-away shock expansion sets in at about 400 ms after core bounce. The shock front is visible as a bluish, enveloping line, and the structures inside are semi-transparent isosurfaces for chosen values of the plasma entropy per nucleon. The color coding of these surfaces corresponds to the radial velocity as given by the color bar. The white sphere visible in the upper right panel and faintly also in the lower left panel is the surface of the new-born NS corresponding to a density of $10^{11} \text{ g cm}^{-3}$. At the end of the simulation the shock has reached a diameter of about 2000 km and expands with a velocity of $\sim 3500 \text{ km s}^{-1}$ (Figure from Melson et al, 2015a, © The American Astronomical Society)

$$\rho_0 = \frac{\dot{M}}{4\pi R_s^2 |v_0|} \quad (11)$$

are the velocity (nearly free-fall) and density, respectively, of the collapsing matter ahead of the shock, M is the mass of the accreting, nascent NS, and $\beta_{\rho} = \rho_s \rho_0^{-1}$ the ratio of postshock to preshock density (Janka, 2001). A higher mass accretion rate therefore requires a bigger postshock pressure to stabilize the shock at a given radius (equality relation in Eq. 9) or to initiate outward shock expansion according to the inequality condition in Eq. (9).

On the other hand, a higher mass accretion rate enhances the total luminosity of electron neutrinos and antineutrinos,

$$L_{\nu_e} + L_{\bar{\nu}_e} = 2\beta_1 L_{\nu_x} + \beta_2 \frac{GM\dot{M}}{R_{\text{ns}}}. \quad (12)$$

Here the first term on the rhs represents the contribution from neutrinos diffusing out of the high-density core of the NS. It is expressed in terms of the luminosity of one species of heavy-lepton neutrinos ($\nu_x = \nu_\mu, \bar{\nu}_\mu, \nu_\tau, \text{ or } \bar{\nu}_\tau$). The second term stands for the accretion component, i.e., for energy that is radiated away by ν_e and $\bar{\nu}_e$ produced in the fresh inflow of matter settling onto the NS surface at radius R_{ns} . Equation (12) assumes steady-state conditions (i.e., the mass-flow rate arriving at the NS surface is the same as the accretion rate \dot{M} ahead of the shock), and the parameters have the values of $\beta_1 = 1$ and $\beta_2 \approx 0.5\text{--}1$ (Müller and Janka, 2014). According to Eq. (12), a higher mass-accretion rate enhances the neutrino luminosity and therefore also the heating behind the shock by the reabsorption of some of the radiated neutrinos in the processes of Eqs. (6) and (7).

Two different effects associated with the mass infall of the collapsing stellar core therefore rival each other concerning their influence on the shock evolution: a higher mass accretion rate means a larger ram pressure, damping the shock expansion, and it also leads to stronger neutrino heating, supporting shock expansion. Which of these two effect wins, and whether the neutrino-driven mechanism leads to a successful SN explosion, is a quantitative question and sensitive to the detailed structure of each individual progenitor star. The neutrino-driven mechanism is therefore not “robust” in the sense that success can be taken for granted for all massive SN progenitors once it has been demonstrated to work for selected cases.

Recent self-consistent 3D simulations, which for the first time include energy-dependent neutrino transport treatments, were able to obtain successful explosions for some progenitors above $10 M_\odot$ (namely for stars of 11.2, 15, 18, 20, $27 M_\odot$, and $15 M_\odot$ with rotation by Takiwaki et al, 2012, 2014; Lentz et al, 2015; Müller, 2016; Melson et al, 2015a; Roberts et al, 2016; Janka et al, 2016, respectively), see Fig. 5 for an example. The results, though slightly less optimistic than 2D simulations, still back up the neutrino-driven mechanism and suggest its viability in principle. Even if it does not produce explosions in other investigated cases, the neutrino mechanism seems to fail only marginally.

Still, however, full-scale 3D models are not finally conclusive and require improvements in several aspects. For example, they still lack sufficient (some more, some less) numerical resolution for convergence on the description of the turbulent flow in the postshock layer, employ a variety of (different) approximations for the 3D neutrino transport, omit important microphysics, obtain explosions only with special and not generally accepted assumptions such as rapid rotation (Janka et al, 2016) or nonstandard modifications of the neutrino opacities (Melson et al, 2015a), and start from spherically symmetric initial conditions instead of the multi-dimensional flow that perturbs the convective burning shells around the iron core already prior to collapse (Couch et al, 2015; Müller et al, 2016b; Müller, 2016). It is well possible that the neutrino mechanism will work well and can explain the observational properties (e.g., explosion energies and radioactive yields) for a wide range of massive progenitors once all these remaining deficiencies of current models have been removed. It is also possible, however, that important physics is still missing, for example new phenomena in the nuclear sector (e.g., stronger nucleon-correlation effects in the neutrino opacities than currently considered) or associated with particle

and neutrino physics (e.g., neutrino-flavor oscillations or a sterile neutrino) inside of the new-born NS.

3 Physics of the Neutrino-driven Mechanism

Meanwhile, based to a large extent on the education obtained from continually improved numerical studies, a rather detailed picture of the crucial ingredients and of their interplay in the neutrino-driven mechanism has been worked out. In this Section the current understanding of the physics of neutrino-powered explosions is briefly reviewed.

3.1 Neutrino Heating

Neutrinos deposit energy behind the stalled bounce shock mainly through the absorption of ν_e and $\bar{\nu}_e$ by neutrons and protons, respectively (Eqs. 6 and 7). Energy transfer by scattering reactions of neutrinos and antineutrinos of all flavors with electrons, positrons, and nucleons, by neutrino-antineutrino annihilation, and by neutrino interactions with light nuclei (deuterons, tritons, ${}^3\text{He}$ and α -particles) altogether contribute to the neutrino heating on a much lower level (much less than 10%).

The formation of a postshock layer where neutrinos effectively deposit energy can be easily understood by considering the heating and cooling rates associated with the dominant processes. Neutrino absorptions (Eqs. 6 and 7) dump energy in the stellar plasma outside of the neutrinospheres at a rate per nucleon of

$$q_{\nu}^+ \approx 110 \cdot \left(\frac{L_{\nu_e,52} \langle E_{\nu_e,15}^2 \rangle}{r_7^2 s_{r,\nu_e}} Y_n + \frac{L_{\bar{\nu}_e,52} \langle E_{\bar{\nu}_e,15}^2 \rangle}{r_7^2 s_{r,\bar{\nu}_e}} Y_p \right) \left[\frac{\text{MeV}}{\text{s} \cdot \text{nucleon}} \right], \quad (13)$$

while the inverse processes of ν_e and $\bar{\nu}_e$ emission by electron and positron captures on free nucleons extract energy from the stellar medium at a rate of per nucleon of

$$q_{\nu}^- \approx 145 \left(\frac{k_B T}{2 \text{MeV}} \right)^6 \left[\frac{\text{MeV}}{\text{s} \cdot \text{nucleon}} \right]. \quad (14)$$

In the latter expression the assumption is used that the sum of neutron and proton abundances is unity, $Y_n + Y_p = 1$. Moreover, it is assumed that the electron and positron degeneracy parameters, $\eta_{e^\pm} = \mu_{e^\pm}/(k_B T)$ (where μ_{e^\pm} are the chemical potentials), are small: $\eta_{e^-} = -\eta_{e^+} \approx 0$. This approximation is good in the shock-heated layers because the electron (number) fraction $Y_e = n_e/n_b$ (n_e and n_b being the electron and baryon number density, respectively) and thus the electron degeneracy is rather low and e^\pm pairs are abundant. In Eq. (14), k_B is Boltzmann's constant

and T is measured in Kelvin. In Eq. (13), r_7 is the radius in 10^7 cm, the neutrino luminosities L_{ν_i} are normalized to 10^{52} erg s $^{-1}$, and the mean squared neutrino energies, $\langle E_{\nu_i}^2 \rangle$, are given in units of $(15 \text{ MeV})^2$. The quantities s_{r,ν_i} in the denominators are the so-called flux factors, which account for the fact that not all neutrinos move radially outwards when they stream through the medium still close outside of the neutrinospheres. The neutrino quantities L_{ν_i} , $\langle E_{\nu_i}^2 \rangle$, and s_{r,ν_i} are calculated from the neutrino phase space occupation function $\mathcal{F}_{\nu_i}(\mathbf{r}, E, \mathbf{n}, t)$ at spatial point \mathbf{r} at time t (\mathbf{n} is the unit vector of the neutrino momentum corresponding to energy E) according to

$$L_{\nu_i}(\mathbf{r}, t) = \frac{c}{(hc)^3} \int_{A_r} dA_r \int_0^\infty dE E^3 \int_{4\pi} d\Omega \mathbf{n} \cdot \mathbf{n}_r \mathcal{F}_{\nu_i}(\mathbf{r}, E, \mathbf{n}, t), \quad (15)$$

$$\langle E_{\nu_i}^2 \rangle(\mathbf{r}, t) = \mathcal{E}^{-1} \int_0^\infty dE E^5 \int_{4\pi} d\Omega \mathcal{F}_{\nu_i}(\mathbf{r}, E, \mathbf{n}, t), \quad (16)$$

$$s_{r,\nu_i}(\mathbf{r}, t) = \mathcal{E}^{-1} \int_0^\infty dE E^3 \int_{4\pi} d\Omega \mathbf{n} \cdot \mathbf{n}_r \mathcal{F}_{\nu_i}(\mathbf{r}, E, \mathbf{n}, t), \quad (17)$$

where \mathbf{n}_r is the outward normal vector on a sphere of radius $r = |\mathbf{r}|$, $A_r = 4\pi r^2$ is the area of the sphere, dA_r a surface element on this sphere, and \mathcal{E} a normalization factor defined by $\mathcal{E} = \int_0^\infty dE E^3 \int_{4\pi} d\Omega \mathcal{F}_{\nu_i}(\mathbf{r}, E, \mathbf{n}, t)$.

Equations (15)–(17) are depicted for the general 3D case. In a nonspherical situation q_{ν}^+ and q_{ν}^- of Eqs. (13) and (14), respectively, should be considered as averages over spheres at radii r . The scalar s_{r,ν_i} is the radial component of the flux factor \mathbf{s}_{e,ν_i} , which relates the neutrino energy density with the local neutrino energy-flux density: $\mathbf{F}_{e,\nu_i} = c \mathbf{s}_{e,\nu_i} \varepsilon_{\nu_i}$, where

$$\varepsilon_{\nu_i} = \frac{1}{(hc)^3} \int_0^\infty dE E^3 \int_{4\pi} d\Omega \mathcal{F}_{\nu_i}(\mathbf{r}, E, \mathbf{n}, t), \quad (18)$$

$$\mathbf{s}_{e,\nu_i}(\mathbf{r}, t) = \mathcal{E}^{-1} \int_0^\infty dE E^3 \int_{4\pi} d\Omega \mathbf{n} \mathcal{F}_{\nu_i}(\mathbf{r}, E, \mathbf{n}, t). \quad (19)$$

The neutrino-heating rate depends on the local neutrino energy density, ε_{ν_i} , and the mean squared energy $\langle E_{\nu_i}^2 \rangle$. In order to coin the heating rate in a form familiar from the 1D case, the neutrino luminosity (Eq. 15) through the sphere of radius r was introduced in Eq. (13) by integrating the projected energy flux, $\mathbf{F}_{e,\nu_i} \cdot \mathbf{n}_r$, over the surface of the sphere. The flux factor s_{r,ν_i} is typically close to 0.25 near the neutrinosphere and gradually approaches unity when the neutrino distributions get more and more forward peaked in the limit of free streaming with increasing distance from the neutrinosphere. Angle-dependent transport, i.e., solving the Boltzmann transport equation, is necessary to accurately determine the spectral and angular distributions of the neutrinos.

Since outside of the neutrinosphere the neutrino luminosities and mean squared energies are only weakly dependent on the radius and at some distance away from the neutrinosphere also the flux factor is already close to its asymptotic value of unity, Eq. (13) implies that the neutrino-heating rate drops roughly with r^{-2} . In

contrast, the neutrino-cooling rate (Eq. 14) decreases much more steeply with approximately r^{-6} because of a $T \propto r^{-1}$ decline in radiation-pressure dominated low-density plasma behind the shock (Janka, 2001). Since at a time later than a few 10 ms after core bounce, the postshock medium becomes sufficiently tenuous for radiation-dominated conditions to prevail, the steep profile of the cooling rate allows for the appearance of a crossing point of $q_{\bar{\nu}}^+$ and $q_{\bar{\nu}}^-$, outside of which neutrino heating dominates neutrino cooling. The corresponding radius is called “gain radius” (Bethe and Wilson, 1985), R_g , and satisfies the relation

$$R_g T_g^3 \propto \sqrt{L_{\nu} \langle E_{\bar{\nu}}^2 \rangle}, \quad (20)$$

when $T_g = T(R_g)$, and the total luminosity and mean squared energy of electron-flavor neutrinos are introduced according to

$$L_{\nu} = L_{\nu_e} + L_{\bar{\nu}_e}, \quad (21)$$

$$\langle E_{\bar{\nu}}^2 \rangle = \frac{L_{\nu_e} \langle E_{\nu_e}^2 \rangle + L_{\bar{\nu}_e} \langle E_{\bar{\nu}_e}^2 \rangle}{L_{\nu_e} + L_{\bar{\nu}_e}}, \quad (22)$$

using $Y_n \approx Y_p \approx 0.5$ and $s_{r,\nu_e} \approx s_{r,\bar{\nu}_e} \approx 1$ as reasonable approximations in Eq. (13). The gain radius R_g thus separates a neutrino-cooling layer between the neutrinosphere and this radius from a neutrino-heating layer (“gain layer”) between R_g and the shock front (at R_s).

Appreciable amounts of energy can be transferred to the stellar gas in the gain layer. Considering a mass $M_g = \int_{R_g}^{R_s} dV \rho(\mathbf{r})$ in this region and employing Eqs. (13), (21), and (22), one estimates a total energy deposition rate by ν_e plus $\bar{\nu}_e$ absorption of

$$\begin{aligned} Q_{\nu}^+ &= q_{\nu}^+ \frac{M_g}{m_u} \\ &\sim 6.3 \times 10^{51} \frac{\text{erg}}{\text{s}} \left(\frac{\langle E_{\bar{\nu}}^2 \rangle}{(15 \text{ MeV})^2} \right) \left(\frac{L_{\nu}}{6 \times 10^{52} \text{ erg/s}} \right) \\ &\quad \left(\frac{M_g}{0.01 M_{\odot}} \right) \left(\frac{R_g}{100 \text{ km}} \right)^{-2}, \end{aligned} \quad (23)$$

which corresponds to a heating efficiency $(Q_{\nu}^+ - Q_{\nu}^-)/L_{\nu}$ of typically 5–10% when energy losses by the re-emission of neutrinos from the gain layer (with an integrated rate of Q_{ν}^-) are taken into account.

3.2 Competition of Time Scales

The energy deposited by neutrinos in the gain layer does not only depend on the product of luminosity and mean squared energy of the radiated neutrinos (the “heating functional”) but also on the mass that is neutrino-heated (Eq. 23) and on the

duration matter is exposed to the neutrino heating. In the spherically symmetric (1D) case, the matter accreted by the stalled shock flows radially inward through the gain layer. This implies that the residence time of the matter in the gain layer is given by the advection time

$$t_{\text{adv}} = \int_{R_g}^{R_s} \frac{dr}{|v_r(r)|} \sim \frac{R_s - R_g}{|v_1|}, \quad (24)$$

which measures how long it takes the accretion flow (with radial velocity $v_r(r)$) to move from R_s to R_g (Janka and Keil, 1998; Janka et al, 2001; Thompson et al, 2005). In Eq. (24) the last expression on the rhs side is a rough approximation invoking the postshock velocity $v_1 = v_0 \beta_\rho^{-1}$ (with β_ρ being the density jump in the shock and v_0 the preshock velocity of Eq. 10). Instead of using Eq. (24) with (mass-weighted, angle-averaged) mean values of the relevant quantities in the multi-dimensional case, where the postshock layer is stirred by violent non-radial motions due to SASI activity and buoyant flows, the dwell time of matter in the gain region can be represented by the more general expression (Buras et al, 2006; Marek and Janka, 2009)

$$t_{\text{dwell}} \approx \frac{M_g}{\dot{M}}, \quad (25)$$

which relates the mass in the gain layer, M_g , with the mass accretion rate \dot{M} through the shock and (for conditions near steady state) through the gain radius. Equation (25) thus measures the time the (stationary) accretion flow needs to replace all the mass in the gain layer by fresh matter, independent of the detailed flow structure in this layer.

For discussing neutrino heating as a driver of the explosion, the time matter is exposed to the heating must be compared to the time that is required to deposit the energy that brings matter to the threshold of becoming unbound in the gravitational field of the NS. For this to be reached, neutrinos have to transfer the equivalent of the total binding energy of the matter in the gain layer, which takes a time of

$$t_{\text{heat}} = \frac{\int_{R_g}^{R_s} dV \rho(\mathbf{r}) |e_{\text{tot}}(\mathbf{r})|}{Q_v^+ - Q_v^-} = \frac{E_{\text{tot,g}}}{Q_v^+ - Q_v^-} \sim \frac{m_u |e_{\text{tot}}(R_g)|}{q_v^+ - q_v^-}, \quad (26)$$

where $e_{\text{tot}}(\mathbf{r})$ is the total (i.e., internal plus kinetic plus gravitational plus magnetic) specific (i.e., per unit of mass) energy of the stellar plasma at spatial point \mathbf{r} and $E_{\text{tot,g}}$ the total energy in the gain region.

Runaway shock expansion requires that $t_{\text{heat}} \lesssim t_{\text{dwell}} \approx t_{\text{adv}}$. This condition implies that the matter behind the stalled shock can absorb from neutrinos an energy equivalent to its net gravitational binding energy during the time interval the gas stays in the gain layer, i.e., before it is advected into the cooling layer and loses its energy again by efficient radiation of neutrinos. Since the shock begins to expand due to the pressure increase associated with the growing thermal energy in the gain region, t_{adv} increases further and a favorable situation for explosive runaway ensues. Numerical simulations confirm this necessary (though not sufficient) condition for

the onset of a SN explosion by the neutrino-driven mechanism (see, e.g., Buras et al, 2006; Marek and Janka, 2009; Fernández, 2012; Summa et al, 2016; Janka et al, 2016), and Müller (2016) argued that other heuristic explosion criteria proposed in the literature, e.g. the antesononic condition of Pejcha and Thompson (2012), have basically a very similar physical meaning.

Multi-dimensional flows in the postshock layer due to hydrodynamic instabilities such as convective overturn and the SASI have a multitude of favorable effects for the development of an explosion. They lead to an increase of the shock radius by pushing the shock farther out (see Sect. 3.4) and thus allow for a larger mass in the gain layer; they stretch the dwell time of matter in the wider gain region and therefore increase the neutrino heating and the heating efficiency *for a fixed value of the neutrino-heating functional* (i.e., of the product of luminosity and mean squared energy of ν_e plus $\bar{\nu}_e$; Eqs. 21 and 22) compared to the 1D case; they reduce energy losses from the gain layer through the re-emission of neutrinos because neutrino-heated, high-entropy matter can become buoyant and rise outward to cooler regions farther away from the gain radius; and they additionally reduce the heating time scale by raising the total energy of the gas in the gain layer due to kinetic energy of non-radial flows and turbulent motions. All these effects in combination facilitate the onset of explosions in more than one spatial dimension for lower values of the heating functional than in spherical symmetry (see also Sect. 3.5) and enable neutrino-driven explosions to become more energetic for given neutrino luminosity and spectra.

3.3 Energetics of Neutrino-driven Explosions

The fact that runaway shock expansion sets in when the neutrino heating and dwell time scales become equal means that the postshock matter expands away from the gain radius as soon as it has absorbed an energy roughly equal to its binding energy in the gravitational potential of the NS. This implies that at least some of the matter in the gain layer begins to acquire positive total (i.e., internal plus kinetic plus gravitational) energy e_{tot} . As a consequence —unless a very intense neutrino flash were able to superheat the matter in the gain layer within a short instant of time, creating an electron-positron pair-plasma fireball—, neutrinos do *not* deliver the net energy of the SN blast, although their energy deposition is crucial to enable the onset of the explosion.

Rather than being transferred by neutrino interactions, the excess energy that the SN ejecta will possess after their escape from the gravitational trough of the compact remnant, is provided by the release of nuclear binding energy in the recombination of free nucleons to α -particles and iron-group nuclei. This recombination sets in when the postshock matter expands to a radius exceeding roughly $R_{\text{diss}} \sim 240$ km (Eq. 5 with $M \sim 1.5 M_{\odot}$), i.e., at a distance from the neutrinosphere where neutrino heating has already become inefficient. Nuclear recombination releases $E_{\text{nuc}} = 7\text{--}8.8$ MeV per nucleon, depending on whether helium or iron-group nuclei form. Nu-

merical simulations, however, show that effectively $\gtrsim 5$ MeV per nucleon contribute to the net positive energy that matter can carry away to infinity.

Therefore the explosion energy of neutrino-driven SNe depends crucially on the amount of material that is expelled by neutrino heating and releases its nuclear recombination energy during outward expansion. At the onset of the explosion, the mass in the gain layer can be estimated as

$$M_g = \int_{R_g}^{R_s} dV \rho(r) \sim \frac{\dot{M} R_s^{3/2}}{\sqrt{2GM}} \beta_\rho \ln\left(\frac{R_s}{R_g}\right) \quad (27)$$

$$\approx 6.3 \times 10^{-3} M_\odot \left(\frac{\dot{M}}{0.2 M_\odot/\text{s}}\right) \left(\frac{R_s}{200 \text{ km}}\right)^{3/2} \left(\frac{M}{1.5 M_\odot}\right)^{-1/2}, \quad (28)$$

where we made use of Eqs. (10,11), assumed a density profile following $\rho(r) \propto r^{-3}$ in the radiation-dominated, nearly isentropic (because convectively mixed) post-shock layer (Janka, 2001), and applied $\beta_\rho \ln(R_s R_g^{-1}) \approx 7$ and typical values also for the other quantities in Eq. (28). With a recombination energy E_{nuc} between ~ 5 MeV and at most 8.8 MeV per nucleon and a mass M_{heat} for the neutrino-heated ejecta, we therefore estimate an energy release of

$$E_{\text{rec}} = E_{\text{nuc}} \left(\frac{M_{\text{heat}}}{m_u}\right) \approx (9.6 \dots 17.0) \times 10^{50} \text{ erg} \left(\frac{M_{\text{heat}}}{0.1 M_\odot}\right) \quad (29)$$

$$\approx (6.0 \dots 10.7) \times 10^{49} \text{ erg} \left(\frac{M_g}{6.3 \times 10^{-3} M_\odot}\right)$$

$$\approx (6.0 \dots 10.7) \times 10^{49} \text{ erg} \left(\frac{\dot{M}}{0.2 M_\odot/\text{s}}\right) \left(\frac{R_s}{200 \text{ km}}\right)^{3/2} \left(\frac{M}{1.5 M_\odot}\right)^{-1/2}, \quad (30)$$

where we introduced Eq. (28) in the second and third line. From Eq. (30) it is evident that the mass in the gain layer at the beginning of the explosion is not sufficient to explain explosions significantly more energetic than about 10^{50} erg. A SN energy of 10^{51} erg requires a mass of $\sim 0.1 M_\odot$ of neutrino-heated ejecta. However, when the explosion sets in, additional matter—typically several times the original mass of the gain layer—expands from the cooling layer through the gain radius into the gain layer, for which reason the mass in the gain layer rises steeply once the SN shock takes off. Moreover, multi-dimensional simulations point to a long period (possibly lasting for more than a second) of continued accretion after the onset of the explosion, during which a considerable fraction of the accreted matter is re-ejected after having absorbed energy from neutrinos in the vicinity of the gain radius (Marek and Janka, 2009; Müller, 2015; Bruenn et al, 2016; Müller et al, 2016a). Finally, also the neutrino-driven wind that is expelled by neutrino heating from the surface of the new-born NS contributes to the mass of neutrino-heated ejecta and to the explosion energy through its wind power. The energy of neutrino-driven explosions can therefore be expressed as

$$E_{\text{exp}} \approx E_{\text{nuc}} \left(\frac{M_{\text{heat}}}{m_{\text{u}}} \right) + E_{\text{burn}} - E_{\text{bind}} \quad (31)$$

with

$$M_{\text{heat}} = f M_{\text{g}} + \dot{M} t_{\text{acc}} \eta_{\text{ej}} + M_{\text{wind}}. \quad (32)$$

In Eq. (32), $f \geq 1$ is a numerical factor accounting for the additional mass shifting from the cooling layer into the gain layer at the onset of the explosion, t_{acc} is the period of time over which accretion with (an approximately constant) rate \dot{M} continues beyond the start of the explosion, $\eta_{\text{ej}} \leq 1$ is the fraction of the accreted matter that gets re-ejected after having absorbed energy from neutrinos, and M_{wind} is the mass of the neutrino-driven wind blown off the NS surface. For simplicity, in Eq. (31) the effective recombination energy per nucleon (i.e., after subtracting the remaining gravitational binding effects) is assumed to be the same for all three components of the neutrino-heated ejecta, although there can be some variation in time as well as between the different components. The term E_{burn} adds the extra energy provided by explosive nuclear burning in progenitor layers that are heated and (directly) ejected by the outgoing SN shock, and E_{bind} corrects for the gravitational binding energy of these layers. Equation (31) is approximate also because it assumes that there is a well defined transition between the phase of simultaneous accretion and mass rejection on the one hand and direct outward acceleration of shock-heated matter on the other hand.

The different terms in Eqs. (31) and (32) are strongly dependent on the progenitor star, with the mass in the gain layer given by Eqs. (27,28) as a function of the mass-accretion rate, \dot{M} , which itself depends on the compactness of the progenitor core. The neutrino-wind mass M_{wind} scales steeply with the neutrino luminosity of the new-born NS and its mass, because $\dot{M}_{\text{wind}} \propto L_{\nu}^a M^{-b}$ with $a = 2.4 \dots 2.5$ and $b = 2$ for Newtonian gravity (Qian and Woosley, 1996) and $b = 2.7 \dots 3.1$ for general-relativistic potential (Thompson et al, 2001). In the case of O-Ne-Mg-core progenitors a non-negligible fraction of the explosion energy comes from the neutrino-driven wind (third term on the rhs in Eq. 32), whereas massive iron-core progenitors with large core-compactness values obtain most of their explosion energy from the second term on the rhs of Eq. (32).

Energy from explosive nuclear fusion of silicon and oxygen to nickel releases at most about 0.8 MeV per nucleon and thus provides an energy of

$$E_{\text{fusion}} \lesssim 0.8 \text{ MeV} \left(\frac{M_{\text{Ni}}}{m_{\text{u}}} \right) \approx 1.54 \times 10^{50} \text{ erg} \left(\frac{M_{\text{Ni}}}{0.1 M_{\odot}} \right). \quad (33)$$

In core-collapse SNe nuclear fusion never contributes more than roughly 10% of the explosion energy: low-mass progenitors eject very little nickel ($\lesssim 10^{-2} M_{\odot}$, some of which stems from nucleon recombination in expanding, neutrino-heated plasma) so that less than $\sim 10^{49}$ erg are produced by explosive burning, while in high-mass progenitors less than about $\sim 10^{50}$ erg result from nuclear burning (SN 1987A, for example, was the explosion of a $15\text{--}20 M_{\odot}$ star with an energy of $\sim 1.3 \times 10^{51}$ erg and a ^{56}Ni mass of about $0.07 M_{\odot}$).

In neutrino-powered SNe neutrinos transfer the energy to matter that expands away from the heating layer as soon as it has absorbed enough energy to overcome its gravitationally bound state. Therefore the explosion energy scales roughly with the mass M_{heat} of the neutrino-heated matter (Eqs. 31,32). For this reason the order of magnitude of the explosion energy is, very approximately, also determined by the gravitational binding energy of the progenitor layers around the mass cut that separates ejecta and compact remnant. (Note that the collapse of these layers proceeds nearly adiabatically.) This insight explains the wide spread of observationally inferred energies of core-collapse SNe from less than $\sim 10^{50}$ erg for the lowest-mass SN progenitors to more than $\sim 10^{51}$ erg for high-mass stars like the progenitors of SN 1987A and Cassiopeia A (excluding hypernovae with their more extreme energies). It also allows one to understand why the energy scale of core-collapse SNe is similar to that of Type Ia SNe, whose energies are of the order of the gravitational binding energy of the exploding white dwarfs. In both cases one considers degenerate stellar objects or cores, and in both cases the gravitational binding energy is dominated by matter near the surface of these degenerate bodies (see also Burrows, 2013).

The expansion of neutrino-heated matter away from the region of strong heating provides a natural feedback mechanism that regulates the explosion energy of neutrino-powered SNe to be of the order of the gravitational binding energy of the progenitor shells around the mass cut. This is a distinct difference from the case of hypernovae, whose much larger energy scale points to a fundamentally different explosion mechanism that does not only lack such a regulating feedback, but which is also much more efficient than the neutrino mechanism, and in which it is not stellar ejecta that store the energy from the beginning. Since neutrino-antineutrino annihilation was found not to be effective enough to create a pair-plasma fireball, the energy reservoir of hypernova explosions is probably the huge rotational energy of a NS spinning near its break-up limit or of a black hole-accretion torus configuration, whose rotation energy can be highly efficiently tapped by strong magnetic fields. The energy at the beginning is therefore electromagnetic energy, not thermal energy of baryonic matter. An interesting question is whether SN cases exist where neutrinos *and* magnetic fields both contribute to powering the explosion.

In this context it is still necessary to answer the question how energetic neutrino-driven explosions can be. Is the neutrino-driven mechanism able to explain SN explosions with observed energies around 10^{51} erg or more? 1D hydrodynamic simulations with parametric neutrino “engines” as well as analytic-parametric treatments suggest that neutrino-driven explosions could be as energetic as $\sim 2 \times 10^{51}$ erg (Sect. 4.4 and Fig. 13). Reliable answers of these questions, however, can only be obtained by 3D simulations with a self-consistent modeling of all physics ingredients. From the discussion in this Section it is clear that a crucial requirement for powerful explosions is that the SN blast has to be launched sufficiently early, i.e. at a time when the mass-accretion rate of the shock is still sufficiently high to guarantee that the gain layer contains an appreciable amount of matter and that a sufficiently large gas mass can be channeled through the neutrino-heating region also by post-explosion accretion and re-ejection (Eqs. 27,28,31,32).

3.4 The Role of Non-radial Flows — “Turbulence”

As discussed in Sect. 3.2, multi-dimensional effects, i.e., non-radial mass motions in the postshock layer, have a variety of explosion-supporting effects. The growth conditions and saturation properties of such non-radial, turbulent flows associated with convection and the SASI have been a matter of vivid debate. A concise recent review of the relevant arguments and literature can be found in Müller (2016).

Buoyancy-driven convective instability is fostered by the negative entropy gradient established by neutrino heating in the gain layer. Its growth rate in the linear regime is of the order of the Brunt-Väisälä frequency ω_{BV} :

$$\omega_{\text{BV}}^2 = g \left(\frac{1}{\rho} \frac{\partial \rho}{\partial r} - \frac{1}{\rho c_s^2} \frac{\partial P}{\partial r} \right) \quad (34)$$

(P , ρ , c_s , and $g \approx GM r^{-2}$ are the local pressure, density, sound speed, and gravitational acceleration, respectively; convective instability holds when $\omega_{\text{BV}}^2 > 0$). Outward rise of buoyant plumes in the inward moving accretion flow of the postshock layer, however, requires a somewhat stricter condition to be fulfilled (unless initial perturbations are sufficiently large; Foglizzo et al, 2006):

$$\chi \equiv \int_{R_g}^{R_s} dr \frac{\omega_{\text{BV}}}{|v_r(r)|} \sim \frac{t_{\text{adv}}}{t_{\text{conv}}} \gtrsim 2 \dots 3. \quad (35)$$

Here, all quantities (ω_{BV} , v_r , gain radius R_g , and shock radius R_s) refer to the angle- and time-averaged averaged mean flow (Fernández et al, 2014), t_{adv} is given by Eq. (24), and $t_{\text{conv}} \sim \langle \omega_{\text{BV}}^{-1} \rangle$ is the convective growth time scale, volume averaged over the gain layer.

The linear growth rate of SASI shock deformation modes due to an amplifying advective-acoustic cycle in the accretion flow between stalled accretion shock and NS surface is given by (Foglizzo et al, 2007; Scheck et al, 2008):

$$\omega_{\text{SASI}} = \frac{\ln |\mathcal{Q}|}{t_{\text{cyc}}}. \quad (36)$$

Here, \mathcal{Q} is the cycle efficiency ($|\mathcal{Q}| > 1$ for SASI growth) and

$$t_{\text{cyc}} = \int_{R_0}^{R_s} \frac{dr}{|v_r(r)|} + \int_{R_0}^{R_s} \frac{dr}{c_s(r)} \sim t_{\text{adv}} \quad (37)$$

the duration of the cycle as the sum of sound-travel time (second, sub-dominant term because $c_s(r) \gg |v_r(r)|$) and advection time between shock radius and a cycle-coupling radius R_0 , which is located in the flow-deceleration region between NS radius (R_{ns}) and gain radius. (The last inequality is therefore very approximative since $R_0 \sim R_g$). According to Eq. (36) the SASI growth rate scales inversely with the cycle period. SASI activity is therefore expected to be strongest during retraction

phases of the accretion shock, whereas its development is less favored when the shock expands and $\chi \gtrsim 3$ becomes fulfilled for efficient growth of convection.

The impact of these hydrodynamic instabilities on the shock propagation and the neutrino-driven mechanism depends on the saturation amplitude of turbulent velocity fluctuations, volume-averaged over the gain layer (indicated by the angle brackets):

$$\langle \delta v \rangle = \sqrt{\langle (v_r - \bar{v}_r)^2 \rangle + \langle (v_\theta - \bar{v}_\theta)^2 \rangle + \langle (v_\phi - \bar{v}_\phi)^2 \rangle} = \sqrt{\frac{2E_{\text{turb,g}}}{M_g}}, \quad (38)$$

where \bar{v}_r , \bar{v}_θ , and \bar{v}_ϕ are angular averages of the r , θ , and ϕ components of the velocity, respectively, over spherical shells, and $E_{\text{turb,g}}$ is the turbulent kinetic energy in the gain layer. Müller (2016) argued, and presented evidence, for similar saturation amplitudes, $\langle \delta v \rangle \sim K |\langle v_r \rangle|$ with a constant K in the same ballpark for both convective and SASI regimes despite different saturation mechanisms for the two instabilities.

In the case of convection, saturation occurs when the volume-integrated net neutrino-heating rate, $Q_v = Q_v^+ - Q_v^-$, and the convective luminosity in the gain region roughly balance each other, which implies a quasi-stationary state of buoyant driving and turbulent dissipation (Murphy et al, 2013). Based on this assumption, Müller and Janka (2015) and Müller (2016) deduced a scaling relation between $\langle \delta v \rangle$ and the average net neutrino-heating rate, $q_v = q_v^+ - q_v^-$, in the gain region:

$$\langle \delta v \rangle = C \left[\frac{q_v}{m_u} (R_s - R_g) \right]^{1/3} = C \left[\frac{Q_v}{M_g} (R_s - R_g) \right]^{1/3} \quad (39)$$

(with C being a numerical coefficient that depends on the dimension and the velocity components included in the definition of $\langle \delta v \rangle$). Müller (2016) showed that this can be converted to the form $\langle \delta v \rangle \sim K |\langle v_r \rangle|$ with K of the order of unity.

In the case of the SASI, a similar scaling law is obtained by assuming that the SASI amplitude saturates when the kinetic energy of coherent SASI motions is dissipated in turbulent flows through parasitic instabilities such as Kelvin-Helmholtz shear vortices (Guilet et al, 2010). By equating the SASI growth rate (Eq. 36) with the average shear rate in the gain layer, Müller (2016) derived

$$\langle \delta v \rangle \sim \ln |\mathcal{Q}| |\langle v_r \rangle|, \quad (40)$$

which seems to capture the basic dynamics of the postshock flow in multi-dimensional simulations for a roughly constant value of the quality factor $|\mathcal{Q}| > 1$.

These considerations are only qualitative order-of-magnitude estimates. The relative importance of convection and the SASI in building up and storing non-radial kinetic energy in the postshock layer, their detailed roles in the revival of the stalled SN shock, and the exact differences between 2D and 3D dynamics remain topics of vivid debate (for reviews, see Janka et al 2016, Müller 2016, and Foglizzo et al 2015; for examples of conflictive points of view, see also Burrows et al 2012; Fernández

2015; Cardall and Budiardja 2015). Controversies are often based on simplified numerical models, but conclusive answers for the SN-core dynamics on the way to a successful explosion require fully self-consistent 3D simulations.

The leverage of different effects associated with non-radial mass motions in the gain layer on the behavior of the SN shock (see Sect. 3.2) must be pinpointed by a careful quantitative analysis of the properties of the postshock turbulence and its consequences for energy and momentum transport, turbulent pressure, or dissipative heating (Murphy and Meakin, 2011), for example by means of a Reynolds decomposition of the momentum stress tensor $\rho \mathbf{v} \otimes \mathbf{v}$ (Murphy et al, 2013; Couch and Ott, 2015; Radice et al, 2016).

Instead, Müller and Janka (2015) proposed a simple, schematic framework to account for the overall impact of postshock turbulence on the shock evolution in a (quasi-)stationary accretion situation, which proved to be quite successful in direct comparison to 2D and 3D simulations in the convective as well as SASI regimes. Motivated by the recognition that the squared turbulent Mach number,

$$\langle \text{Ma}^2 \rangle = \frac{\langle \delta v^2 \rangle}{\langle c_s^2 \rangle} = \frac{2E_{\text{turb,g}}/M_g}{\langle c_s^2 \rangle} \quad (41)$$

with

$$\langle c_s^2 \rangle = \frac{1}{M_g} \int_{R_g}^{R_s} dV \rho(\mathbf{r}) c_s^2(\mathbf{r}) \quad (42)$$

being the mass-weighted average of the squared sound speed in the gain layer, plays a pivotal role because it reflects the violence of aspherical mass motions in the gain layer and determines the amplitude of shock oscillations, they considered the effect of turbulent stresses as an additional isotropic pressure contribution: $P_{\text{turb}} \approx \rho \langle \delta v^2 \rangle$ (see also Murphy et al, 2013; Couch and Ott, 2015; Radice et al, 2015). This turbulent pressure can be expressed in terms of the gas pressure P as $P_{\text{turb}} \approx \rho c_s^2 \langle \text{Ma}^2 \rangle \approx \frac{4}{3} \langle \text{Ma}^2 \rangle P$, because $P = \Gamma^{-1} \rho c_s^2$ with $\Gamma \approx \frac{4}{3}$ in the radiation-dominated environment of the gain layer.

Replacing the gas pressure P by $P + P_{\text{turb}} = (1 + \frac{4}{3} \langle \text{Ma}^2 \rangle) P$ on the lhs of the equality relation of Eq. (9) and applying the gain condition (Eq. 20) in the form $P_g^{3/2} \propto L_v \langle E_v^2 \rangle R_g^{-2}$ for the radiation-dominated plasma in the gain layer ($P \propto T^4$, $\rho \propto T^3 \propto r^{-3}$; Janka, 2001), Müller and Janka (2015) derived a relation for the shock-stagnation radius:

$$R_s \propto \frac{(L_v \langle E_v^2 \rangle)^{4/9} R_g^{16/9}}{M^{2/3} M^{1/3}} \xi_{\text{turb}}^{2/3}. \quad (43)$$

Here the factor

$$\xi_{\text{turb}} = 1 + \frac{4}{3} \langle \text{Ma}^2 \rangle \geq 1 \quad (44)$$

accounts for the increase of the average shock radius caused by the additional turbulent pressure support of the shock against the ram pressure of the infalling preshock matter. With $\xi_{\text{turb}} = 1$ the 1D case is recovered (Janka, 2012). Similarly, centrifugal

support associated with rapid rotation can lead to an expansion of the shock. This can be taken into account by introducing another correction factor $\xi_{\text{rot}}^{-2/3}$ in Eq. (43) with ξ_{rot} being defined as

$$\xi_{\text{rot}} = \sqrt{1 - \frac{j_0^2}{2GM R_s}} \leq 1, \quad (45)$$

where j_0 is the specific angular momentum (averaged on spherical shells) of matter ahead of the shock (for the derivation, see Janka et al, 2016). Also perturbations in the convective silicon and oxygen-burning shells of the pre-collapse progenitor can have a healthy influence on the shock-stagnation radius by enhancing the turbulent activity in the postshock layer (Couch and Ott, 2013; Müller and Janka, 2015). Corresponding modifications of Eq. (43) were discussed by Müller et al (2016b).

3.5 Universal Critical Luminosity Condition

In Sect. 2.3.2 the road to explosion was described as a tight competition of preshock ram pressure of the infalling matter and postshock heating by the neutrino luminosity of the new-born NS. For both competing effects the mass-accretion rate \dot{M} of the stalled shock is of pivotal importance. Burrows and Goshy (1993) found (by semi-analytic analysis in 1D) that stationary accretion solutions are not possible for electron-flavor neutrino luminosities above a critical limit $L_{\nu, \text{crit}}(\dot{M})$ (see also Yamasaki and Yamada, 2006; Pejcha and Thompson, 2012). Fernández (2012), applying 1D hydrodynamic simulations, and Janka (2012) with simple analytic considerations showed that this critical luminosity condition is roughly compatible with the time-scale criterion $t_{\text{adv}}/t_{\text{heat}} \geq 1$ for runaway shock expansion. Using approximations for both time scales based on Eqs. (24) and (26), blackbody assumptions ($L_{\nu} \propto R_{\text{ns}}^2 T_{\nu}^4$) for the neutrino emission (following Burrows and Goshy, 1993), and Eq. (43) with $\xi_{\text{turb}} = 1$ and $R_g \propto R_{\text{ns}}$ for the shock-stagnation radius, Janka (2012) derived for the critical luminosity limit:

$$L_{\nu, \text{crit}}(\dot{M}) \propto \beta_{\rho}^{-2/5} \dot{M}^{2/5} M^{4/5}. \quad (46)$$

This relation reproduces the functional behavior obtained by Burrows and Goshy (1993) very well. The numerical factor of the scaling relation becomes $(5 \dots 6) \times 10^{52} \text{ erg s}^{-1}$ for individual luminosities of ν_e or $\bar{\nu}_e$, when $\beta_{\rho} \sim 10$, $\dot{M} = 1 M_{\odot}/\text{s}$, and a NS mass of $M = 1.5 M_{\odot}$ are used, and slightly varies with the choice of other involved parameters.

Müller and Janka (2015) generalized the critical luminosity condition, based on the time-scale criterion $t_{\text{adv}} = t_{\text{heat}}$ for the onset of shock runaway, to a critical condition for the heating functional $L_{\nu} \langle E_{\nu}^2 \rangle$, including also the effects of turbulent stresses in the postshock flow by employing Eq. (43) for the shock-stagnation radius. Further adding the possible effects of rotation into the treatment, Janka et al (2016)

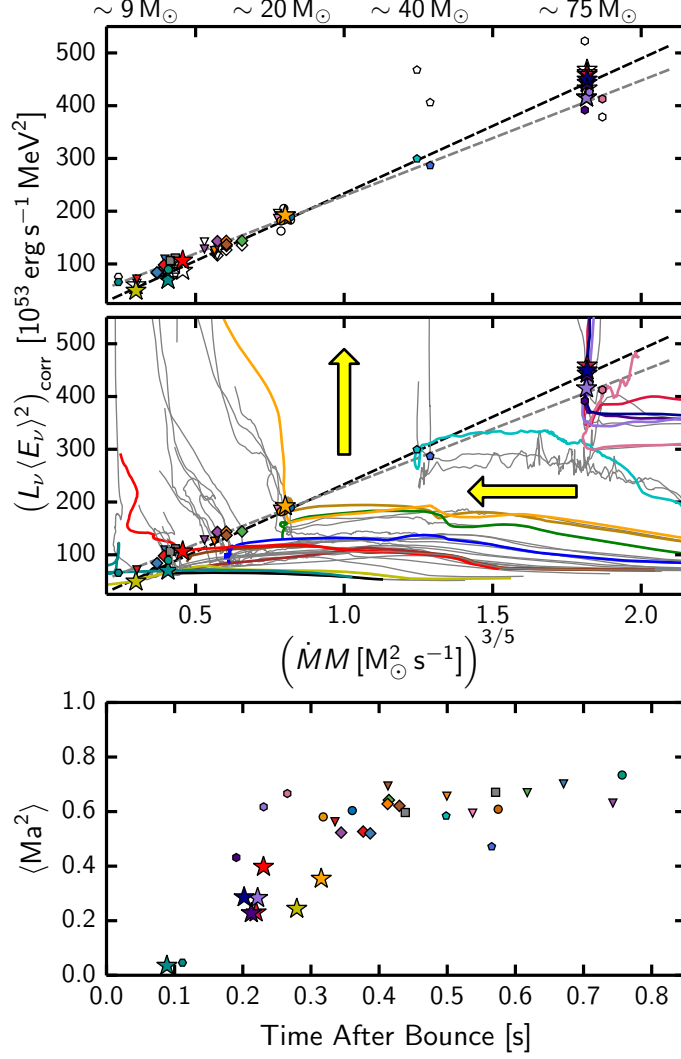


Fig. 6 Critical condition for the heating functional at the threshold for runaway shock expansion. The upper two panels display by dashed lines the critical relation between $(L_\nu \langle E_\nu^2 \rangle)_{\text{crit,corr}}$ and $(\dot{M} M)^{3/5}$ at the onset of shock runaway (Eq. 50). The black dashed line was obtained by a least-squares fit to the critical points of a set of non-rotating and rotating 3D models (stars), the gray dashed line depicts the least-squares fit for a set of 2D models, also with and without rotation (all non-star, smaller symbols). Open symbols correspond to the locations of the uncorrected values of $(L_\nu \langle E_\nu^2 \rangle)_{\text{crit}}$ (Eq. 47). The middle panel shows the evolution tracks (the post-bounce evolution proceeds from right to left, indicated by yellow arrows) of exploding and non-exploding 2D (thin, gray lines) and 3D models (thick, colored lines). Exploding models cross the corresponding critical line by turning upward. The bottom panel depicts average squared turbulent Mach numbers in the gain layer (Eq. 41) at the time when runaway shock expansion begins. (Figure courtesy of Alexander Summa)

obtained:

$$(L_V \langle E_V^2 \rangle)_{\text{crit}} \propto (\dot{M} M)^{3/5} |\bar{e}_{\text{tot,g}}|^{3/5} R_g^{-2/5} \xi_{\text{turb}}^{-3/5} \xi_{\text{rot}}^{6/5} \equiv (\dot{M} M)^{3/5} \xi_g, \quad (47)$$

with $\bar{e}_{\text{tot,g}}$ being the average, mass-specific binding energy in the gain layer:

$$\bar{e}_{\text{tot,g}} = \frac{E_{\text{tot,g}}}{M_g}. \quad (48)$$

In Eq. (47) the time-dependent quantity ξ_g , defined as

$$\xi_g \equiv |\bar{e}_{\text{tot,g}}|^{3/5} R_g^{-2/5} \xi_{\text{turb}}^{-3/5} \xi_{\text{rot}}^{6/5}, \quad (49)$$

subsumes all gain-layer related properties. Following Summa et al (2016), ξ_g can be used to correct $L_V \langle E_V^2 \rangle$ for variations of the time evolution of gain radius, binding energy, nonradial (turbulent) postshock flows, and rotation, which cause time- and model-dependent variations of the critical condition in addition to the basic dependence on the NS mass M and the shock-accretion rate \dot{M} . Doing so yields a universal relation for the heating functional at the threshold for shock runaway:

$$(L_V \langle E_V^2 \rangle)_{\text{crit,corr}} \equiv \frac{1}{\xi_g / \xi_g^*} (L_V \langle E_V^2 \rangle)_{\text{crit}} \propto (\dot{M} M)^{3/5}. \quad (50)$$

An arbitrary constant ξ_g^* normalizes the correction factor relative to a chosen reference model, for which ξ_g^* is evaluated at the time when $t_{\text{adv}}/t_{\text{heat}} = 1$.

Figure 6 displays the critical points in the $(L_V \langle E_V^2 \rangle)_{\text{crit,corr}} - (\dot{M} M)^{3/5}$ -plane for a large set of full-scale 2D and 3D SN simulations in a wide mass range from the low-mass end ($< 10 M_\odot$) to heavy progenitors around $75 M_\odot$. All points line up nicely on straight curves, suggesting that Eq. (50) captures the basic physics of shock runaway very well. Moreover, the best-fit relations (least-squares fits) for 2D and 3D models (grey and black dashed lines, respectively) are nearly identical, suggesting that Eq. (50) defines a universal critical condition that holds for non-rotating as well as rotating core-collapse conditions (nearly) independently of dimension.

The bottom panel in Fig. 6 shows the squared turbulent Mach number $\langle \text{Ma}^2 \rangle$, averaged over the gain layer (Eq. 41), at the time when runaway shock expansion sets in. All successful 3D models show runaway shock expansion rather early, and some of them exhibit the tendency to do so even slightly earlier than the corresponding 2D cases. The fact that they do so despite possessing considerably lower values of $\langle \text{Ma}^2 \rangle$ at the onset of criticality seems to imply a considerably higher critical heating functional $(L_V \langle E_V^2 \rangle)_{\text{crit}}$ (Eq. 47) in 3D, since in this case ξ_{turb} is lower (Eq. 44). (Note that this difference would not show up in the critical curve in Fig. 6, because the critical heating functional there is normalized by applying the factor ξ_g^{-1} .) Simulations, however, do not comply with this expectation but instead show that the critical conditions of 2D and 3D models are rather close, a finding which points to subtle hydrodynamical effects that can aid explosions in 3D despite lower overall values of $\langle \text{Ma}^2 \rangle$ in the gain layer (see the discussion in sect. 3.3.4 of Müller, 2016).

One possibility is that in 3D kinetic energy in the gain layer is efficiently stored in spiral SASI modes Fernández (2015). Such coherent flows do not behave like turbulent velocity fluctuations and, consequently, do not add to ξ_{turb} as defined by us. Instead, they decrease the specific binding energy of the gain layer, $|\bar{e}_{\text{tot,g}}|$ and therefore also ξ_{g} according to Eq. (49). This effect on the critical condition is similar to the influence of moderately rapid rotation, in which case centrifugal effects in the infall region ahead of the SN shock are negligibly small (therefore $\xi_{\text{rot}} \approx 1$; Eq. 45), but the rotational kinetic energy in the postshock region lowers the value of $|\bar{e}_{\text{tot,g}}|$ (Janka et al, 2016).

4 Astrophysical Implications of Neutrino-driven explosions

The understanding of the neutrino-driven mechanism and the hydrodynamical modeling of explosions have meanwhile matured enough to make predictions of observables and to study implications of neutrino-powered SN. In this Section some recent developments in this context will be summarized.

4.1 Neutrino and Gravitational-wave Signals

Both neutrinos and gravitational waves play an important role as messengers that can directly probe the dynamics and, in the case of neutrinos, also the thermodynamics of the SN core.

There is a variety of effects that can imprint characteristic features on the luminosity evolution and the spectral properties of the neutrino signal, such as the prominent ν_e burst produced by electron captures at the moment of shock breakout from the neutrinosphere; the subsequent accretion luminosities of ν_e and $\bar{\nu}_e$ during the shock-stagnation phase, which are determined by the mass accretion rate \dot{M} and therefore by the compactness of the progenitor core; and the cooling and deleptonization emission of neutrinos and antineutrinos of all flavors during the Kelvin-Helmholtz phase of the new-born NS, which depend on the mass of the compact remnant and its high-density equation of state with possible phase transitions in the super-nuclear regime.

Similarly, time-dependent centrifugal deformation induced by rapid rotation as well as violent mass motions associated with convective overturn and SASI activity in the neutrino-heating layer and convection inside of the NS lead to variations of the mass-quadrupole moment and therefore gravitational-wave radiation. While the reader is referred to the special chapters on neutrinos and gravitational waves from core-collapse SNe for more information and details, two interesting phenomena are briefly mentioned here, because they are relevant for the pre-explosion diagnostics of neutrino-driven SNe in the case of neutrino and gravitational-wave measurements connected to a future galactic SN.

Large-amplitude SASI sloshing and spiral motions of the postshock layer induce fluctuations of the mass-accretion rate of the NS and, correspondingly, show up as pronounced, quasi-periodic modulations of the radiated neutrino luminosities and mean energies with amplitudes of more than 10% and phase-synchronized variations of up to 1 MeV, respectively (Tamborra et al, 2013, 2014b). Though dependent on the viewing angle, these variations with a typical frequency of t_{cyc}^{-1} (see Eq. 37) are likely to be detectable by IceCube and Hyper-Kamiokande for a SN anywhere in the Galaxy, if SASI activity precedes the onset of the explosion in this event. Similarly, also the gravitational-wave emission is modulated with characteristic spectral peaks around frequencies t_{cyc}^{-1} and $2t_{\text{cyc}}^{-1}$ (Andresen et al, 2016), which, in the lucky case of a SN that is not too distant, could be measured by existing interferometric instruments (Kuroda et al, 2016).

In the 3D SN simulations by the Garching group a new, stunning feature was discovered in the neutrino emission: a lepton-number self-sustained asymmetry (LESA), in which the lepton-number emission (ν_e minus $\bar{\nu}_e$) develops a large dipole component some 150–200 ms after bounce, whose amplitude can exceed the monopole of the lepton-number flux, and whose direction remains rather stationary or drifts only slowly on time scales much longer than those that are typical of mass motions due to SASI activity and convective overturn (Tamborra et al, 2014a). While the hemispheric difference of the lepton-number flux is huge (even to the extent that the ν_e and $\bar{\nu}_e$ fluxes can dominate in opposite hemispheres), the individual fluxes of ν_e and $\bar{\nu}_e$ exhibit hemispheric differences only of order 10%, and the total ν_e plus $\bar{\nu}_e$ flux as well as the total neutrino flux (including heavy-lepton neutrinos) feature large-scale directional variations only on the level of percent.

This new LESA phenomenon is present in all 3D simulations of the Garching group, but the amplitude of the lepton-number emission dipole is smaller in the case of rotation and even more suppressed when the NS spins faster. LESA can be traced back to a neutrino-hydrodynamical instability in the convective layer inside of the NS (Janka et al, 2016). It could have important consequences for neutrino-flavor oscillations in SN cores, SN neutrino detection, neutrino-induced SN nucleosynthesis, and NS kicks.

4.2 Neutron Star Kicks and Anisotropic Nucleosynthesis

Because of momentum conservation in the rest frame of the progenitor star, asymmetric mass ejection of a SN or asymmetric neutrino emission can lead to a recoil acceleration of the NS that is left behind by the explosion (e.g., Janka and Müller, 1994; Lai et al, 2001).

The hydrodynamic instabilities that precede and foster the onset of neutrino-driven SN explosions are associated with a considerable redistribution of matter and energy around the nascent NS. Corresponding asymmetries of the mass distribution or velocity field of the innermost SN ejecta exert anisotropic hydrodynamic (i.e., gas-pressure mediated) and gravitational forces that push or pull the compact rem-

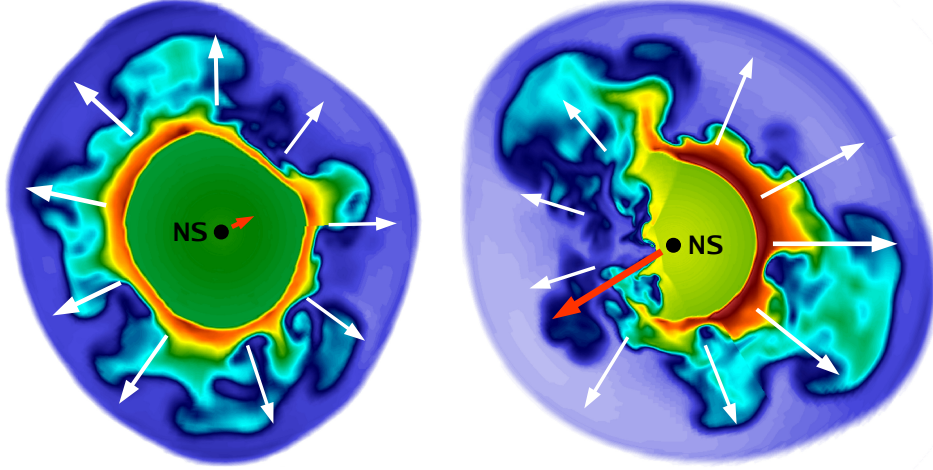


Fig. 7 NS kick by asymmetric SN explosions. The color coding shows entropy distributions in cross sectional planes of 3D simulations of neutrino-driven explosions for two different $15 M_{\odot}$ stars about 1.4 s after core bounce (Wongwathanarat et al, 2013). Dark blue are low-entropy, dense ejecta, bright blue, green, yellow, and red are high-entropy, neutrino-heated ejecta that partly rise in low-density Rayleigh-Taylor plumes. The white arrows indicate the momentum of the expanding ejecta, the red arrow the NS kick direction and magnitude. The NS is gravitationally pulled by the clumps of dense, slow ejecta opposite to the direction of the stronger blast-wave expansion. *Left:* Nearly spherical explosion with small NS kick ($\sim 100 \text{ km s}^{-1}$). *Right:* Highly aspherical explosion with large dipolar and quadrupolar ejecta inhomogeneities and a stronger shock expansion towards the right side. Here the NS receives a large kick ($\sim 550 \text{ km s}^{-1}$) mediated by the gravitational attraction of the less rapidly expelled, dense clumps on the left side.

nant in the direction opposite to the stronger explosion (Fig. 7). Gravitation as a long-range interaction is very efficient in accelerating the NS over time scales of several seconds and therefore much longer than asymmetric accretion is likely to last after the SN blast has taken off. Even only a small hemispheric mass-ejection difference Δm , expelled on the one side and missing on the other in an otherwise homogeneous ejecta shell, can yield an appreciable NS kick, v_{ns} , by its asymmetric gravitational attraction (“gravitational tug-boat mechanism” for NS acceleration; Wongwathanarat et al, 2013):

$$v_{\text{ns}} \approx \frac{2G\Delta m}{r_i v_s} \approx 540 \frac{\text{km}}{\text{s}} \left(\frac{\Delta m}{10^{-3} M_{\odot}} \right) \left(\frac{r_i}{100 \text{ km}} \right)^{-1} \left(\frac{v_s}{5000 \text{ km/s}} \right)^{-1}, \quad (51)$$

where r_i and v_s are the initial radius and the expansion velocity of the shell, respectively. A hemispheric mass-ejection asymmetry as small as $10^{-3} M_{\odot}$, expanding with a constant velocity of 5000 km s^{-1} , can thus pull the NS to a velocity of 540 km s^{-1} .

3D simulations by Wongwathanarat et al (2010, 2013) showed that the explosion asymmetries that grow naturally from small initial seed perturbations due to convective and SASI activity in the postshock layer (for an example, see Fig. 8) are

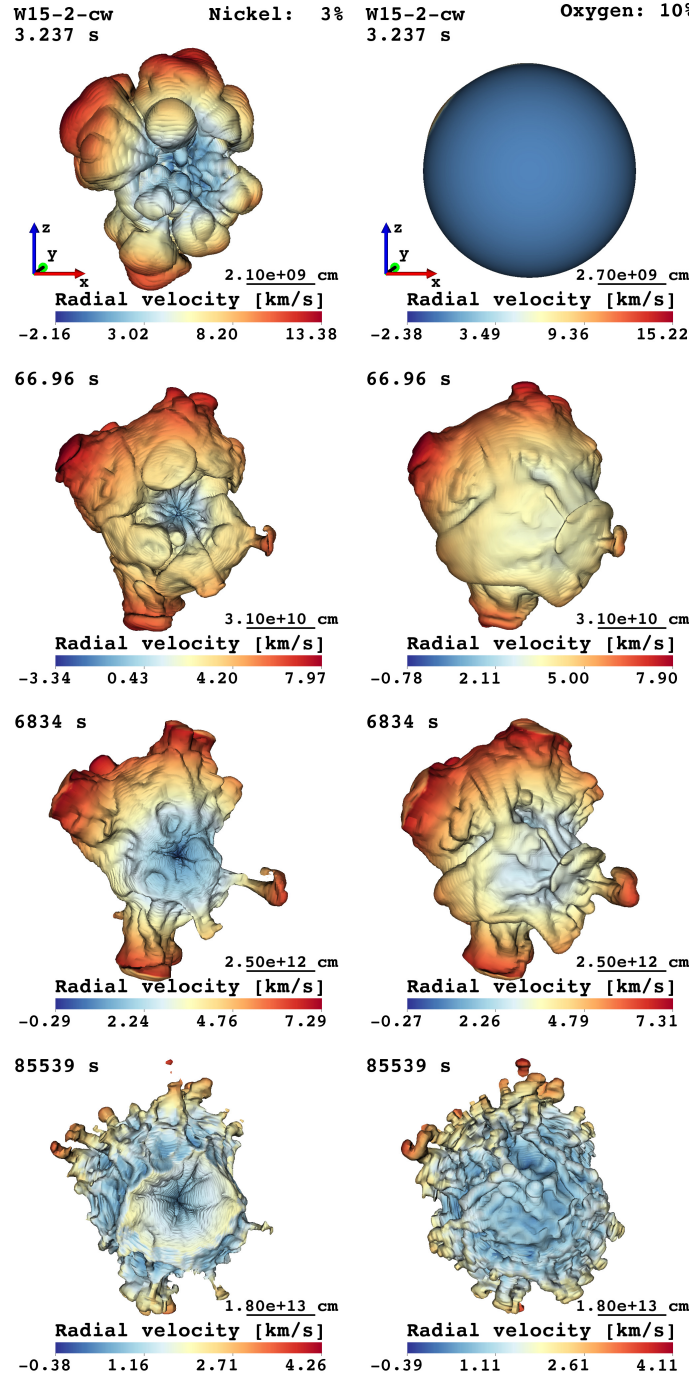


Fig. 8 The first day of a SN. The images from a 3D simulation of a neutrino-driven explosion of a $15 M_{\odot}$ red supergiant (SN IIP) progenitor (Wongwathanarat et al, 2015) show isosurfaces of constant mass fractions of ^{56}Ni (3%; *left*) and oxygen (10%; *right*). The color coding visualizes the radial velocity as given by the color bars. *Top*: Shortly before the SN shock crosses the C-O/He composition interface. *Second row*: Shortly before shock passage through He/H composition interface. The reverse shock from the C-O/He interface has already compressed the nickel plumes. *Third row*: At the time when the reverse shock from the He/H interface hits the most extended nickel fingers. *Bottom*: At shock breakout from the stellar surface. The large-scale high-entropy bubbles of the beginning explosion (*top*) fragment to smaller-scale structures. (Figures courtesy of Annop Wongwathanarat)

sufficiently large to explain NS kicks of several 100 km s^{-1} and, most likely, even beyond 1000 km s^{-1} (as already obtained in 2D simulations by Scheck et al, 2006). Neutrino-driven SN explosions are therefore able to explain the observed space velocities of typically $\sim 200\text{--}500 \text{ km s}^{-1}$ of the majority of young pulsars (see, e.g., Arzoumanian et al, 2002; Hobbs et al, 2005).

Janka (2016) argued that because of momentum conservation a simple relation exists between the NS kick velocity on the one hand and the momentum-asymmetry of the ejecta, α_{ej} , and the explosion energy, E_{exp} , of the SN on the other hand:

$$v_{\text{ns}} = 211 \frac{\text{km}}{\text{s}} \zeta \left(\frac{\alpha_{\text{ej}}}{0.1} \right) \left(\frac{E_{\text{exp}}}{10^{51} \text{ erg}} \right) \left(\frac{M}{1.5 M_{\odot}} \right)^{-1}, \quad (52)$$

where ζ is a numerical factor of order unity. Equation (52) means that the NS kick grows roughly linearly with the explosion energy (or, alternatively, with the relevant ejecta mass, M_{ej}) and with the explosion asymmetry α_{ej} . Both dependences are easy to understand: a more asymmetric and more powerful explosion is able to impart a larger kick to the NS. The momentum asymmetry parameter α_{ej} is determined by the stochastic growth of hydrodynamic instabilities in the postshock

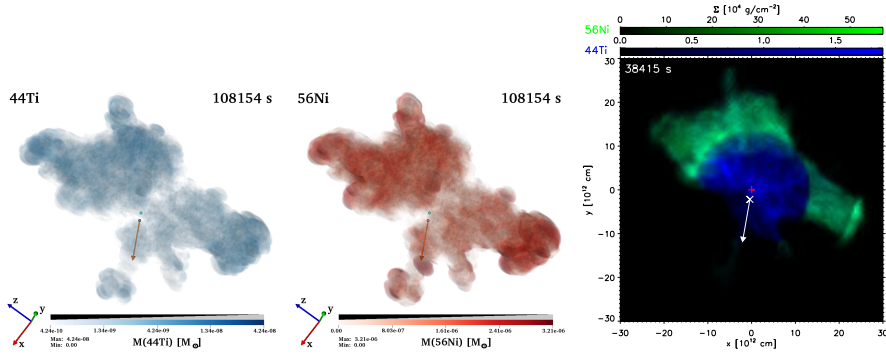


Fig. 9 NS kick and explosive SN nucleosynthesis in a 3D simulation of a highly asymmetric neutrino-driven explosion of a $15 M_{\odot}$ SN IIB progenitor (the same explosion model as shown in Fig. 8 but with a nearly completely stripped hydrogen envelope; Wongwathanarat et al, 2013, 2016). The SN blast ejects heavy elements from silicon to the iron group, which are explosively produced in shock-heated and neutrino-heated matter, preferentially in the direction of the stronger explosion, i.e. opposite to the NS kick direction. The latter is indicated by the red or white arrows pointing downward. The ray-tracing images display the distributions of radioactive ^{44}Ti (left) and ^{56}Ni (middle) more than a day after the initiation of the SN outburst, when the ejecta expand essentially homologously. The largest fingers that are present at this late time originate from the biggest high-entropy bubbles of neutrino-heated matter that dominated the asymmetry at the beginning of the explosion. The right image shows ^{56}Ni (green) and ^{44}Ti (blue) in combination, but assuming that only the outer 50% of the nickel mass are visible. The similarity to the NuSTAR ^{44}Ti map of the Cassiopeia A remnant (Grefenstette et al, 2014) is striking. Iron (most of which is the stable decay product of ^{56}Ni) can be observed only in the reverse-shock heated outer shell of the SN remnant, while ^{44}Ti is seen by its decay activity also in the inner, unshocked volume, concentrated mostly in the hemisphere opposite to the NS kick. (Figure courtesy of Annap Wongwathanarat)

layer, which trigger the onset of an asymmetric explosion. Kick velocities in excess of 1000 km s^{-1} require $\alpha_{\text{ej}} \gtrsim 0.5$ for all other factors in Eq. (52) being unity, which is a rare case but within reach of some published explosion models (e.g., Scheck et al, 2006; Wongwathanarat et al, 2013).

Since in the described hydrodynamical kick scenario the NS velocity vector points away from the stronger explosion, 3D models predict enhanced explosive nucleosynthesis in the hemisphere opposite to the direction of the NS kick (Wongwathanarat et al, 2013). This concerns mostly chemical elements between ^{28}Si and the iron-group, which are significantly or exclusively produced during the SN outburst in the innermost shock-heated and neutrino-heated ejecta. The hemispheric asymmetry of the element distribution increases with the magnitude of the NS kick. Indeed, high-resolution mapping with the NuSTAR X-ray telescope reveals that the spatial distribution of ^{44}Ti in the Cassiopeia A SN remnant is fully compatible with this prediction (Grefenstette et al, 2014). Inspecting the observational information of ^{44}Ti and iron in combination, the geometry and many morphological features of this young gas remnant exhibit amazing resemblance to results that can be obtained in 3D simulations of neutrino-driven explosions (see Fig. 9 and Wongwathanarat et al, 2016).

4.3 Explosion Asymmetries and Large-scale Mixing

Hydrodynamic instabilities do not only play a crucial role during the first second of neutrino-driven SN explosions but also when the shock wave moves out from the stellar core through the mantle and envelope of the disrupted star. Large-scale radial mixing is induced by the growth of Rayleigh-Taylor (RT) mushrooms at the C-O/He and He/H composition-shell interfaces after the passage of the shock. These mixing instabilities destroy the onion-shell structure of the progenitor star by carrying radioactive nuclei and iron-group elements from the innermost layers into the helium and hydrogen shells and, reversely, displace hydrogen from the fast stellar envelope inward into the slowly expanding metal core. The presence of such transport processes was for the first time concluded from observations of SN 1987A, where it was needed to explain the unexpectedly early detection of X-rays and γ -rays from the decay of radioactive isotopes, the smoothness and large width of the light-curve peak, and a variety of velocity-dependent spectral-line features that pointed to clumpiness and inhomogeneities in the SN ejecta (for a review, see Arnett et al, 1989).

The growth of the RT instabilities near the C-O/He and He/H composition-shell interfaces is triggered by crossing density and pressure gradients that are associated with local density maxima in the postshock flow (Chevalier, 1976). These build up when the shock decelerates in the flattening density profiles within composition shells after phases of acceleration in regions with steeper density gradients near the shell interfaces. While the outer edges of the density maxima become RT unstable, their inner edges steepen into strong reverse shocks, which decelerate and compress

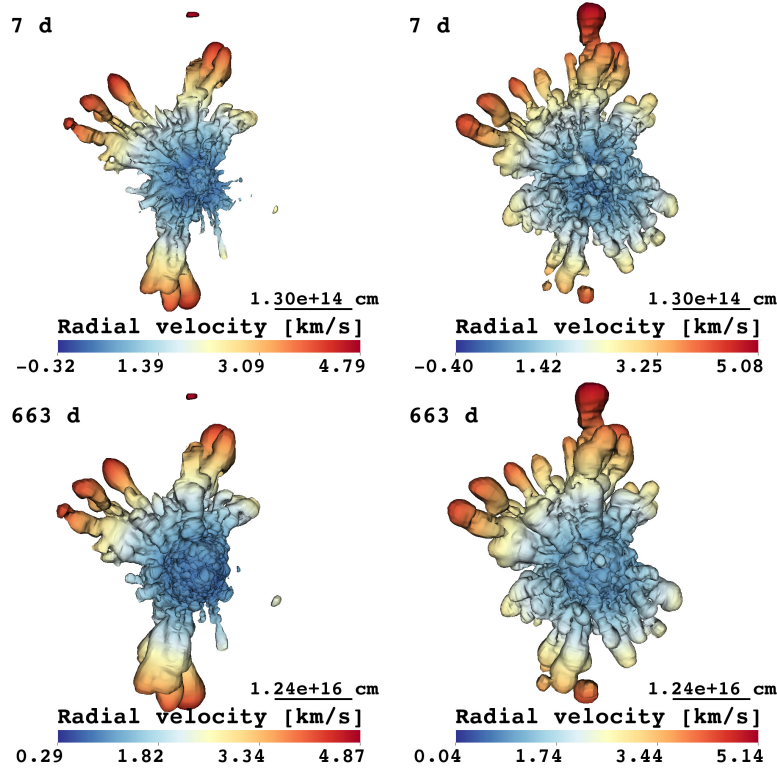


Fig. 10 The first two years of a Type IIP SN. The images are from a 3D simulation that continues the neutrino-driven explosion model shown in Fig. 8 from shock breakout to almost two years later. Isosurfaces of constant mass fractions of 3% for ^{56}Ni (*left*) and 10% for ^{16}O (*right*) are shown (analog to Fig. 8). The color coding denotes radial velocities. *Top*: Structure after the red supergiant has reached the phase of homologous expansion. Notice the significant changes of the geometrical structure and velocity distribution compared to the moment of shock breakout in the bottom images of Fig. 8. *Bottom*: After two years of radioactive heating by ^{56}Ni decay to stable ^{56}Fe . There is minor boosting of the fastest ejecta in the most extended fingers, but quite significant long-time acceleration of the bulk of the ejecta at velocities below $\sim 2000 \text{ km s}^{-1}$. (Figure courtesy of Michael Gabler)

the neutrino-heated and metal-rich inner ejecta when encountering them (Kifonidis et al, 2003).

Kifonidis et al (2006) showed that the RT growth rate is considerably boosted by the initial asymmetries that support the onset of neutrino-driven explosions, and Hammer et al (2010) and Wongwathanarat et al (2015) demonstrated, performing 3D simulations of neutrino-driven explosions continuously from core bounce until shock breakout at the stellar surface, that this interaction of initial and secondary instabilities can facilitate the penetration of ^{56}Ni and ^{44}Ti with high velocities (up to more than 4000 km s^{-1} for the fastest clumps) deep into the hydrogen envelope as well as inward mixing of significant amounts of hydrogen to velocities as

low as $\sim 100 \text{ km s}^{-1}$. For blue supergiant progenitors with compact, small helium cores ($\sim 4\text{--}4.5 M_{\odot}$) both effects in combination are efficient enough to produce a good match of the wide, dome-like shape of the light-curve maximum observed for SN 1987A (Utrobin et al, 2015).

Wongwathanarat et al (2015), however, found that the interaction of initial and secondary instabilities depends extremely sensitively, and in a subtle way, on the detailed density structure of the progenitor star, which determines the acceleration and deceleration phases of the outgoing shock and therefore the RT growth rates in the unstable layers as well as the time when the reverse shocks collide with the material of the expanding metal core. While especially the reverse shock from the He/H interface decelerates the metal-rich ejecta, the secondary RT instabilities enable mixing at the shell interfaces and lead to a fragmentation of the large-scale asymmetries of the early explosion into smaller fingers and filaments (see Fig. 8).

Nevertheless, the largest and most powerful plumes created at the beginning of the neutrino-driven explosion trigger also the strongest growth of the RT instabilities at the composition-shell interfaces, and thus they shape the final morphology of the SN explosion and of the developing SN remnant (see Figs. 9 and 10). The initial explosion asymmetries that are intrinsically connected to the neutrino-driven explosion mechanism must therefore be included in self-consistent hydrodynamic 3D simulations of the SN blast wave from its initiation to the late stages of homologous expansion, if SN models shall be compared to the observational properties of SN explosions and SN remnants. These initial asymmetries can either grow stochastically from (small-scale) random fluctuations, or they might be triggered by large-scale asymmetries in the convective silicon and oxygen burning shells of the progenitor at the onset of core collapse (Burrows and Hayes, 1996; Arnett and Meakin, 2011; Couch and Ott, 2013; Müller and Janka, 2015; Müller et al, 2016b; Müller, 2016).

4.4 Progenitor-explosion-remnant Connection

The compactness parameter ξ_M (Eq. 2) of the progenitor core (M is typically chosen between $1.5 M_{\odot}$ and $2.5 M_{\odot}$) is able to provide crude information about the destiny of a collapsing massive star: explosion as a SN for low compactness or collapse to a black hole (BH) for compactness values above a certain threshold (O’Connor and Ott, 2011). However, neither the best choice of this threshold value nor of the mass M is a priori clear. Also other criteria such as the envelope binding energy (e.g. at $1.5 M_{\odot}$; Burrows et al, 2016) or the mass derivative of the binding energy outside $2 M_{\odot}$ (Sukhbold et al, 2016) may serve as similarly good single-parameter criteria for the stellar “explodability”.

Another problem of the compactness parameter as such a criterion is the fact that its physical significance for the readiness of a star to explode is not obvious. A large compactness value implies a high mass accretion rate \dot{M} of the new-born NS. But, as discussed in Sect. 2.3.2, a high mass accretion rate has two competing effects, namely, a large ram pressure ahead of the shock, which impedes shock expansion,

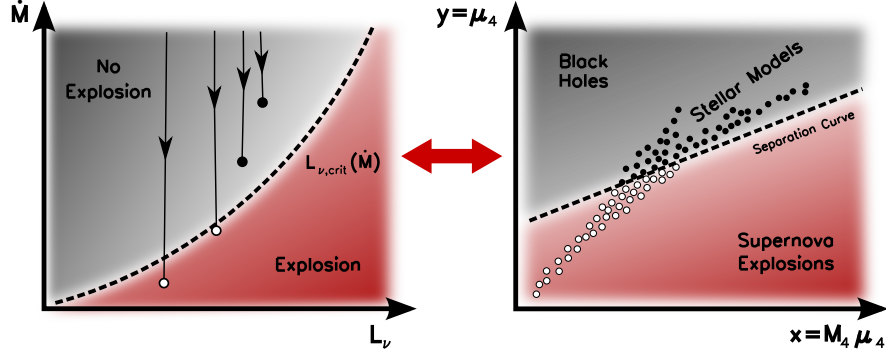


Fig. 11 Two-parameter criterion for the “explodability” of stars. There is a direct correspondence between the L_ν - \dot{M} plane with the critical neutrino-luminosity curve $L_{\nu,\text{crit}}(\dot{M})$ (left) and the 2D-plane spanned by the progenitor-specific parameters of $M_4\mu_4$ and μ_4 , with a separation line between exploding and non-exploding cases (right). In the left plot post-bounce evolution paths of successfully exploding models (white circles) and non-exploding models (black circles) are schematically indicated, corresponding to white and black circles for pre-collapse stellar models in the right plot. Evolution paths of successful cases cross the critical line at some point and the accretion ends after the explosion has taken off. In contrast, the tracks of failing cases never reach the critical condition for launching a runaway expansion of the shock. The symbols in the left plot mark “optimal points” relative to the critical curve, corresponding to the stellar conditions described by the parameters M_4 and μ_4 at the radius where the dimensionless entropy per baryon is $s = 4$. This location is usually decisive for the successful explosion or failure of a progenitor, because the accretion rate drops strongly outside. (Figure from Ertl et al, 2016, © The American Astronomical Society)

and a high accretion luminosity of ν_e and $\bar{\nu}_e$, which enhances the heating behind the shock and increases the chance of an explosion. The compactness ξ_M as a single-parameter criterion does not reflect this ambiguity.

For these reasons Ertl et al (2016) introduced a new criterion involving two parameters that are able to capture the two rivaling effects as the underlying physics of the neutrino-driven explosion mechanism. The first parameter is the normalized mass inside a dimensionless entropy per nucleon of $s = 4$,

$$M_4 \equiv m(s = 4)/M_\odot, \quad (53)$$

which usually is close to the inner boundary of the silicon-enriched oxygen shell. When this location with its density and entropy jump arrives at the stalled shock during core collapse, an explosion is most likely to set in. The second parameter is the mass derivative at this radial position,

$$\mu_4 \equiv \left. \frac{dm/M_\odot}{dr/1000 \text{ km}} \right|_{s=4}. \quad (54)$$

Both of the parameters M_4 and μ_4 are determined from the pre-collapse structure of the progenitor star.

When the progenitor mass shell $m(r)$ (r measures the radius in the progenitor) has collapsed to the stalled shock, one can choose $M = m(r)$ as a suitable proxy of the NS mass, because the layer between NS surface and shock contains only little mass compared to the NS itself. A rough measure of the mass-accretion rate \dot{M} of the shock is then given by the mass-derivative $m'(r) \equiv dm(r)/dr = 4\pi r^2 \rho(r)$ at the progenitor radius r . This is the case because $m'(r)$ can be directly linked to the free-fall accretion rate of matter collapsing into the shock from initial radius r (Ertl et al, 2016):

$$\dot{M} = \frac{dm}{dt_{\text{ff}}} = \frac{dm(r)}{dr} \left(\frac{dt_{\text{ff}}(r)}{dr} \right)^{-1} \approx \frac{2}{3} \frac{r}{t_{\text{ff}}} m'(r), \quad (55)$$

where $t_{\text{ff}} = \sqrt{\pi^2 r^3 / [8Gm(r)]}$ is the free-fall time scale (Woosley and Heger, 2015a). Inspection of large sets of stellar models reveals an extremely tight linear correlation between $m'(r)|_{s=4} \propto \mu_4$ and \dot{M} at the time the $s = 4$ interface falls to the accretion shock. This proves that $\dot{M} \propto m'(r)$ defines the main dependence between the lhs and the rhs of Eq. (55), while the factor $rt_{\text{ff}}^{-1} \propto \sqrt{m(r)r^{-1}} \propto \sqrt{\bar{\rho}r^2}$ (with $\bar{\rho}$ being the average density inside of r) has only a secondary influence. Similarly, at the time when M_4 arrives at the shock, one finds an extremely tight linear relation between $m(r)m'(r)|_{s=4} \propto M_4\mu_4$ and the ν_e plus $\bar{\nu}_e$ luminosity, L_ν , of the NS, for which the accretion luminosity $L_\nu^{\text{acc}} \propto GM\dot{M}R_{\text{ns}}^{-1}$ accounts for the dominant contribution varying between different progenitors. This means that the product $M\dot{M} \propto M_4\mu_4$ captures the main progenitor dependence of the neutrino emission. The dependence on the NS radius is weak since R_{ns} varies weakly between different progenitors at the time when the explosion sets in (Ertl et al, 2016).

According to the concept of a critical luminosity limit $L_{\nu,\text{crit}}(\dot{M})$ for stationary accretion solutions (Eq. 46 and Sect. 3.5), exploding models must pass this threshold luminosity for shock runaway, while non-exploding models should stay below this limit (Fig. 11, left panel; see also Fig. 6, middle panel). Because at the onset of the explosion tight correlations exist between L_ν and $M_4\mu_4$ on the one hand and \dot{M} and μ_4 on the other hand, it may be expected that the critical luminosity curve $L_{\nu,\text{crit}}(\dot{M})$ has a correspondence in the $M_4\mu_4$ - μ_4 plane (see Fig. 11). Exactly such a separation line between exploding and non-exploding models is found in the huge set of hundreds of hydrodynamical SN simulations performed by Ertl et al (2016). A fraction of 97% of all models were found to be classified correctly by the two-parameter criterion with respect to their explosion behavior. A similarly high success rate was reported by Müller et al (2016a), using a completely different, analytical approach for modeling the SN explosions including a parametric description of multi-dimensional effects.

The SN simulations for the large grid of progenitors of different masses between $9M_\odot$ and $120M_\odot$ (partly in steps of $0.1M_\odot$) and different metallicities were not computed in 3D, which is presently not feasible. Instead, the calculations were performed in spherical symmetry (1D), using a parametrized neutrino “engine” that attempts to reproduce the essential physics of the neutrino-driven mechanism. The values of free parameters in the engine model were calibrated such that basic observational properties (explosion energies and nickel yields) of the well studied cases

of SN 1987A on the high-mass side (testing progenitors in the $15\text{--}20 M_{\odot}$ range) and of Crab near the low-mass end ($\sim 9\text{--}10 M_{\odot}$) were reproduced with suitable progenitor models; in the case of SN 1987A also consistency with constraints set by the neutrino detection was requested (see Ugliano et al, 2012; Ertl et al, 2016; Sukhbold et al, 2016).

Applying this neutrino-engine treatment to the progenitor sets for different metallicities, a variegated landscape is obtained, with islands of non-exploding stars alternating with intervals of successful explosions (Figs. 12 and 13). This astonishing result is, on the one hand, connected to the non-monotonic variations of the pre-collapse structure with the ZAMS mass, which is reflected by the core compactness (see Sect. 2.1). On the other hand it is also a consequence of the tight competition between shock-confining ram pressure and shock-pushing neutrino heating, which is characteristic of the neutrino-driven mechanism and which makes successful explosions sensitive to differences in the time-dependent mass-accretion rate as discussed in Sect. 3.2. It is reassuring that this result is not specific to the 1D explosion modeling of Ugliano et al (2012) and Ertl et al (2016), but a rugged landscape was also found by Pejcha and Thompson (2015) for one of their model sets and a different

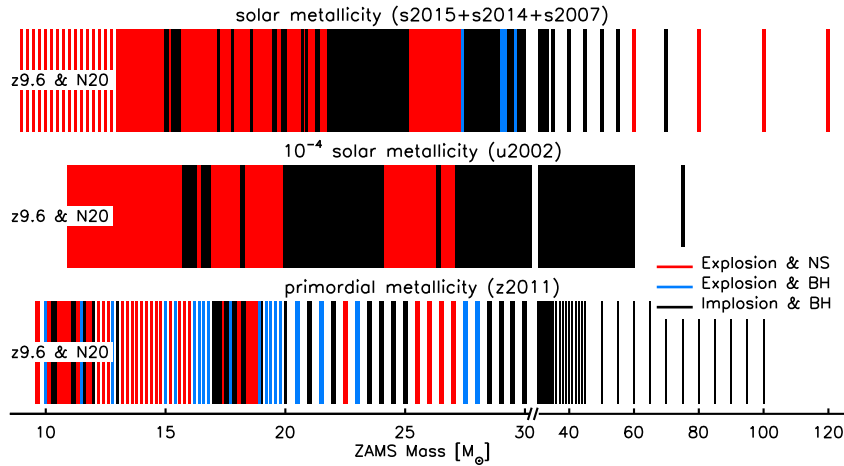


Fig. 12 NS and BH formation cases as function of progenitor ZAMS mass, based on 1D simulations with a calibrated neutrino “engine” (for more details of the modeling approach, see Ertl et al, 2016; Sukhbold et al, 2016). The *upper row* displays results for the compilation of solar-metallicity progenitors used by Sukhbold et al (2016), the *middle row* ultra metal-poor (10^{-4} solar metallicity) models (set u2002) between $11.0 M_{\odot}$ and $75.0 M_{\odot}$ from Woosley et al (2002), and the *bottom row* zero-metallicity models (set z2011) between $9.6 M_{\odot}$ and $100.0 M_{\odot}$ from Heger and Woosley (2010) for the stars above and including $10.3 M_{\odot}$ and from A. Heger (2015, private communication) for the stars with lower masses. Red vertical bars indicate successful explosions with NS formation, black bars BH formation without SN explosion, and blue bars fallback SNe where BHs form due to massive fallback, which leads to more than $3 M_{\odot}$ of baryonic matter in the compact remnant. The rugged landscape of alternating intervals of NS and BH formation events is a consequence of non-monotonicities in the pre-collapse structure of the progenitors as discussed in Sect. 2.1. (Figure courtesy of Thomas Ertl)

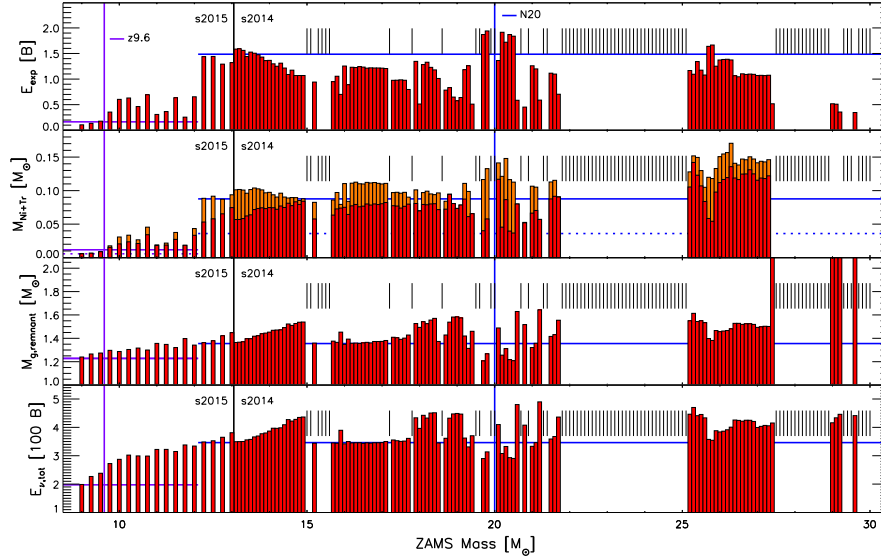


Fig. 13 Explosion and remnant properties as functions of progenitor ZAMS mass for the compilation of single-star, solar-metallicity progenitor models considered by Sukhbold et al (2016). The results are based on 1D simulations with a calibrated neutrino “engine” (for more details, see Ertl et al, 2016; Sukhbold et al, 2016). *Top panel*: explosion energy in bethe ($1 \text{ B} = 10^{51} \text{ erg}$); *second row*: explosively produced and expelled ^{56}Ni in shock-heated and neutrino-heated ejecta (red) with uncertainty range indicated by orange segments of the histogram bars; *third row*: gravitational mass of the NS; *bottom*: total energy release of the new-born NS in neutrinos. In the ^{56}Ni mass and NS mass fallback is taken into account. The vertical black lines in the upper part of each panel indicate cases of direct BH formation without explosion. Five low-energy explosions above $27 M_{\odot}$ are fallback SNe that produce BHs by massive fallback (see also Fig. 12). (Figure courtesy of Thomas Ertl)

approach for determining successful cases. Moreover, a similar behavior was also observed by Müller et al (2016a), who employed a parametric-analytical description for the effects of simultaneous mass accretion and mass ejection as a generically multi-dimensional phenomenon during the post-explosion phase. Because they studied a ten times finer grid of progenitors (i.e., models with a spacing of only $0.01 M_{\odot}$), they did not find mass intervals of pure BH formation below $20 M_{\odot}$ but reported considerable fluctuations in the probability of exploding models within mass intervals of $0.5 M_{\odot}$ width. This lends support to the suggestion by Clausen et al (2015) of a probabilistic description of NS versus BH formation.

All of these results allow for the interesting conclusion that BH birth seems to be possible not only in the collapse of progenitor stars above a certain mass limit, but it can occur with significant probability even below a ZAMS mass of $20 M_{\odot}$. BH formation therefore seems to be more likely than previously thought, maybe as frequent as 25–45% of all core-collapse events (Sukhbold et al, 2016).

Of course, it is by no means clear that such an extreme sensitivity of the explosion to details of the progenitor structure and time-dependent mass-accretion rate

will survive in fully self-consistent 3D simulations, nor is it clear whether the corresponding pre-collapse properties are a robust feature of the progenitor evolution, whose modeling is still performed in 1D with parametric recipes to treat convection and its associated effects.

The explosion calculations for these large sets of stellar models based on the neutrino-driven mechanism allow for many interesting conclusions on the progenitor-explosion-remnant systematics. Comparison of such results with observations can serve as viability check for progenitors as well as explosion physics (for details, see Ugliano et al, 2012; Pejcha and Thompson, 2015; Ertl et al, 2016; Sukhbold et al, 2016; Müller et al, 2016a).

Since the explosion energy scales with the mass of neutrino-heated ejecta (see Sect. 3.3) and determines the mass of shock-heated ejecta, neutrino-driven explosions naturally yield a fairly tight correlation between energy and ^{56}Ni mass as suggested by observations (Sukhbold et al, 2016; Müller et al, 2016a). Moreover, also the ejecta mass and the explosion energy show indications of a correlation (see Müller et al, 2016a). The predicted distribution of NS-birth masses is, overall, compatible with observed NS masses (which would have to be converted to NS birth masses for a proper comparison). Similarly, also the BH masses from the models overlap with the mass distribution of observed BHs in binaries, provided one assumes the hydrogen envelope of the collapsing star gets unbound because of the NS mass decrement associated with neutrino losses before BH formation (Sukhbold et al, 2016). The lack of observed cases between the maximum measured NS mass (around $2 M_{\odot}$) and the minimum discovered BH mass ($\sim 5 M_{\odot}$) naturally emerges in the model sets of Ugliano et al (2012) and Ertl et al (2016), because fallback SNe (whose NSs would accrete solar masses of fallback material and thus could fill the gap) are extremely rare for the investigated solar-metallicity progenitors (their relative importance is considerably higher only in the metal-free progenitor set; see Figs. 12 and 13).

Sukhbold et al (2016) found at most 6–8% of the SN IIP explosions to be connected to progenitors more massive than $20 M_{\odot}$ when they used SN 1987A-calibrated neutrino engines that allow for population-integrated SN nucleosynthesis yields to be in overall agreement with chemogalactic constraints. This may offer an explanation for the rarity of observed high-mass SNe (see Smartt, 2015).

These results for large sets of neutrino-driven explosions in comparison to observations are assuring, but they are still based on rather simple, approximative modeling recipes (either by 1D hydrodynamical or semi-analytic treatments). Full 3D explosion simulations will be needed for more solid conclusions, but tentative studies with 2D calculations (Nakamura et al, 2015) should be taken with great caution, because 2D modeling tends to produce artificial explosions (fostered by the presence of a symmetry axis) and thus is prone to overestimating the readiness of stars to explode. Also the single-star progenitor sets will ultimately have to be supplemented by stellar models from binary evolution. Moreover, it is not clear whether rotation and magnetic fields can be ignored for stars above $\sim 20 M_{\odot}$, which rotate relatively faster at the onset of core collapse (Heger et al, 2005) so that rotational

field amplification during stellar collapse might lead to a non-negligible role of magnetorotational effects in the SN explosions.

5 Conclusions

The theoretical understanding of the physics that plays a role in the neutrino-driven explosion mechanism is meanwhile far advanced, and the picture how the diverse ingredients concur has consolidated (Sect. 3). Hydrodynamical simulations with increasingly better treatment of the neutrino transport and other relevant physics have become feasible in full 3D, but they still require improvements (Sect. 2.3). With growing insight into the essential aspects that play a role in the mechanism, also from the progenitor side, predictions of observational consequences are now possible by means of hydrodynamical explosion models in different dimensions, but also by some (semi-)analytic approaches (Sect. 4).

In spite of this remarkable progress, the 3D simulations are not yet finally conclusive with respect to the possibility of explaining explosions for wider sets of progenitors, with respect to what magnitudes of explosion energies can be achieved by the neutrino-driven mechanism, and with respect to the reasons for differences in the evolution of the stalled shock observed by different groups. For sure, the present generation of 3D simulations calls for further advancements. These include the need of better grid resolution and a reduced influence of discretization noise in the treatments by some groups; the replacement of remaining, different approximations in the transport methods of all groups by more rigorous, fully three-dimensional descriptions; upgrades of the neutrino opacities to state-of-the-art implementations in most of the currently applied 3D codes; and, last but not least, a deeper understanding of the importance and possible role of pre-collapse perturbations in the convective burning shells for a wide range of progenitors (for a review, see Janka et al, 2016).

The long-lasting struggle for robust neutrino-driven explosions, which should prove to be less sensitive to “details” of the input physics or methods applied, still goes on. Because of the difficulties to obtain an ultimately satisfactory solution, some sceptics want to see growing justification for their concerns that advocates of the mechanism are on the wrong track and a paradigm shift is needed.

However, there are arguments in favor of neutrino-driven explosions that should be taken seriously by opponents. There are considerable successes of neutrino-driven SN models such as the fully self-consistent explosions of low-mass progenitors in the $\sim 9\text{--}10 M_{\odot}$ range (Sect. 2.3.1) as well as achievements in reproducing, explaining, and even predicting observed phenomena in SNe and SN remnants (Sect. 4). There is also a blatant lack of convincing alternatives that could account for the far majority of SN explosions. Magnetorotational explosions, a hot candidate for some sceptics of the neutrino mechanism, are excluded because magnetic fields can reach dynamically relevant strength only in the presence of spin rates in stellar cores that are excluded by our present understanding of the angular momen-

tum evolution of stars based on stellar models, observed spins of white dwarfs and NSs, and astroseismological measurements. Stellar models as well as the mentioned observations point to slow core rotation prior to collapse for the far majority of SN progenitors.

In addition to these reasons that refer to solid facts, there are some heuristic arguments that can be brought forward in support of the neutrino mechanism. Why is it so difficult to blow up massive stars? Is this a serious concern and a fundamental problem of the neutrino mechanism, which disfavors its viability? The answer is a clear “no” for the following reasons:

- First, the existence of stellar-mass BHs, which was splendidly confirmed by the first direct measurements of gravitational waves, conveys a simple message: The SN mechanism *is not “robust”*, it must fail in a significant number of cases, maybe more often than previously expected.
- Second, the SN mechanism *must be inefficient*. The reason is the huge discrepancy between the observationally inferred explosion energy of core-collapse SNe and the gigantic amount of available energy that is released in the birth events of NSs and BHs, which exceeds SN energies by more than a factor of 100.
- Third, the SN mechanism *must be self-regulated*, i.e., it must be connected to a sensible feedback effect that quenches the energy input to the explosion as soon as the energy of the expanding ejecta is roughly of the order of the gravitational binding energy in the core of the progenitor star (see Sect. 3.3).

The neutrino mechanism is compatible with these requirements, different from the magnetorotational mechanism, whose energy scale is set by the available rotational energy of the newly formed NS instead of the gravitational binding energy of the progenitor shells that supply the neutrino mechanism with matter to be heated (Sect. 3.3). The absence of a feedback mechanism in the case of magnetorotational explosions can be concluded from the excessive energy released in hypernova explosions (up to $\sim 50 \times 10^{51}$ erg), and the dichotomy between normal SNe and very rare, hyper-energetic events points emphatically to two different explosion mechanisms at work in the two kinds of stellar blasts. (Of course, there is no reason a priori why there should not be a range of overlap, where both mechanisms in synergy drive the explosions of stars.)

All these arguments, of course, are not rigorous and they certainly cannot stand as a proof. But, at least, they make clear that the viability of the neutrino mechanism cannot be rejected on grounds of plausibility arguments that overinterpret and overstate still existing weaknesses of the current numerical models.

Besides further work on the modeling side with the goal to continuously upgrade the simulations for new physics and better numerics, a further consolidation of the paradigm of neutrino-driven explosions requires more empirically testable predictions and the corresponding efforts on the observational side, even before a next Galactic SN will provide measurable neutrino and gravitational-wave signals. In the absence of a single, pivotal observation or measurement that can provide an undisputable proof, one has to strive for as many tests as possible for consistency between predictions derived from neutrino-powered explosions and the events in

nature. Only such a collection of many individual pieces of this highly complex phenomenon (including nucleosynthesis yields, blast-wave energies, NS and BH mass distributions and kicks, explosion asymmetries and mixing, progenitor-SN connections, neutrinos and gravitational waves, etc.) will permit a final breakthrough in assembling the multifaceted picture of how massive stars explode.

Acknowledgements The author is indebted to Thomas Ertl, Michael Gabler, Alexander Summa, and Annop Wongwathanarat for providing graphics used in this article, and to Elena Erastova and Markus Rampp (MPCDF) for their great help in visualizing 3D simulation results. Careful reading of the chapter and comments by Alexander Summa are acknowledged. Research by the author was supported by the European Research Council through an Advanced Grant (ERC-AdG No. 341157-COCO2CASA), by the Deutsche Forschungsgemeinschaft through the Cluster of Excellence “Universe” (EXC-153), and by supercomputing time from the European PRACE Initiative and the Gauss Centre for Supercomputing.

Cross-References

Explosion Physics of Core-Collapse Supernovae
Influence of Non-spherical Initial Stellar Structure on the Core-collapse Supernova Mechanism
Supernovae from Super Asymptotic Giant Branch Stars
Supernovae from Massive Stars (12–100 Msun)
Supernova Remnant Cassiopeia A
Supernova remnant from SN1987A
The Supernova – Supernova Remnant Connection
The Core-collapse Supernova – Black Hole Connection
Neutrino Emission from Supernovae
Neutrino Signatures from Young Neutron Stars
Neutrinos from Core-Collapse Supernovae and Their Detection
Diffuse Neutrino Flux from Supernovae
Gravitational Waves from Core-collapse Supernovae

References

- Akiyama S, Wheeler JC, Meier DL, Lichtenstadt I (2003) The Magnetorotational Instability in Core-Collapse Supernova Explosions. *Astrophys J* 584:954–970, DOI 10.1086/344135, arXiv:astro-ph/0208128
- Alexeyev EN, Alexeyeva LN, Krivosheina IV, Volchenko VI (1988) Detection of the neutrino signal from SN 1987A in the LMC using the INR Baksan underground scintillation telescope. *Physics Letters B* 205:209–214, DOI 10.1016/0370-2693(88)91651-6
- Andresen H, Müller B, Müller E, Janka HT (2016) Gravitational Wave Signals from 3D Neutrino Hydrodynamics Simulations of Core-Collapse Supernovae. *Monthly Notices R Astron Soc*, submitted, 1607.05199

- Arnett D (1967) Mass dependence in gravitational collapse of stellar cores. *Canadian Journal of Physics* 45:1621–1641, DOI 10.1139/p67-126
- Arnett WD (1966) Gravitational collapse and weak interactions. *Canadian Journal of Physics* 44:2553
- Arnett WD, Meakin C (2011) Toward Realistic Progenitors of Core-collapse Supernovae. *Astrophys J* 733:78, DOI 10.1088/0004-637X/733/2/78, 1101.5646
- Arnett WD, Bahcall JN, Kirshner RP, Woosley SE (1989) Supernova 1987A. *Annual Review of Astronomy and Astrophysics* 27:629–700, DOI 10.1146/annurev.aa.27.090189.003213
- Arzoumanian Z, Chernoff DF, Cordes JM (2002) The Velocity Distribution of Isolated Radio Pulsars. *Astrophys J* 568:289–301, DOI 10.1086/338805, astro-ph/0106159
- Baade W, Zwicky F (1934a) Cosmic Rays from Super-novae. *Proceedings of the National Academy of Science* 20:259–263, DOI 10.1073/pnas.20.5.259
- Baade W, Zwicky F (1934b) On Super-novae. *Proceedings of the National Academy of Science* 20:254–259, DOI 10.1073/pnas.20.5.254
- Baade W, Zwicky F (1934c) Remarks on Super-Novae and Cosmic Rays. *Physical Review* 46:76–77, DOI 10.1103/PhysRev.46.76.2
- Bethe HA (1990) Supernova mechanisms. *Rev Mod Phys* 62:801–866, DOI 10.1103/RevModPhys.62.801
- Bethe HA, Wilson JR (1985) Revival of a stalled supernova shock by neutrino heating. *Astrophys J* 295:14–23, DOI 10.1086/163343
- Bionta RM, Blewitt G, Bratton CB, Casper D, Ciocio A (1987) Observation of a neutrino burst in coincidence with supernova 1987A in the Large Magellanic Cloud. *Physical Review Letters* 58:1494–1496, DOI 10.1103/PhysRevLett.58.1494
- Blondin JM, Mezzacappa A (2007) Pulsar spins from an instability in the accretion shock of supernovae. *Nature* 445:58–60, DOI 10.1038/nature05428, arXiv:astro-ph/0611680
- Blondin JM, Mezzacappa A, DeMarino C (2003) Stability of Standing Accretion Shocks, with an Eye toward Core-Collapse Supernovae. *Astrophys J* 584:971–980, DOI 10.1086/345812
- Bruenn SW, Lentz EJ, Hix WR, Mezzacappa A, Harris JA, Messer OEB, Endeve E, Blondin JM, Chertkow MA, Lingerfelt EJ, Marronetti P, Yakunin KN (2016) The Development of Explosions in Axisymmetric Ab Initio Core-collapse Supernova Simulations of 12–25 M Stars. *Astrophys J* 818:123, DOI 10.3847/0004-637X/818/2/123, 1409.5779
- Buras R, Janka HT, Rampp M, Kifonidis K (2006) Two-dimensional hydrodynamic core-collapse supernova simulations with spectral neutrino transport. II. Models for different progenitor stars. *Astron Astrophys* 457:281–308, DOI 10.1051/0004-6361:20054654
- Burrows A (2013) Colloquium: Perspectives on core-collapse supernova theory. *Reviews of Modern Physics* 85:245–261, DOI 10.1103/RevModPhys.85.245, 1210.4921
- Burrows A, Goshy J (1993) A Theory of Supernova Explosions. *Astrophys J Lett* 416:L75, DOI 10.1086/187074
- Burrows A, Hayes J (1996) Pulsar Recoil and Gravitational Radiation Due to Asymmetrical Stellar Collapse and Explosion. *Physical Review Letters* 76:352–355, DOI 10.1103/PhysRevLett.76.352, arXiv:astro-ph/9511106
- Burrows A, Hayes J, Fryxell BA (1995) On the Nature of Core-Collapse Supernova Explosions. *Astrophys J* 450:830–850, DOI 10.1086/176188
- Burrows A, Dolence JC, Murphy JW (2012) An Investigation into the Character of Pre-explosion Core-collapse Supernova Shock Motion. *Astrophys J* 759:5, DOI 10.1088/0004-637X/759/1/5, 1204.3088
- Burrows A, Vartanyan D, Dolence JC, Skinner MA, Radice D (2016) Crucial Physical Dependencies of the Core-Collapse Supernova Mechanism. *Astrophys J*, submitted, 1611.05859
- Cardall CY, Budiardja RD (2015) Stochasticity and Efficiency in Simplified Models of Core-collapse Supernova Explosions. *Astrophys J Lett* 813:L6, DOI 10.1088/2041-8205/813/1/L6, 1509.02494
- Chevalier RA (1976) The hydrodynamics of Type II supernovae. *Astrophys J* 207:872–887, DOI 10.1086/154557

- Clausen D, Piro AL, Ott CD (2015) The Black Hole Formation Probability. *Astrophys J* 799:190, DOI 10.1088/0004-637X/799/2/190, 1406.4869
- Colgate SA, White RH (1966) The Hydrodynamic Behavior of Supernovae Explosions. *Astrophys J* 143:626, DOI 10.1086/148549
- Couch SM, O'Connor EP (2014) High-resolution Three-dimensional Simulations of Core-collapse Supernovae in Multiple Progenitors. *Astrophys J* 785:123, DOI 10.1088/0004-637X/785/2/123, 1310.5728
- Couch SM, Ott CD (2013) Revival of the Stalled Core-collapse Supernova Shock Triggered by Pre-collapse Asphericity in the Progenitor Star. *Astrophys J Lett* 778:L7, DOI 10.1088/2041-8205/778/1/L7, 1309.2632
- Couch SM, Ott CD (2015) The Role of Turbulence in Neutrino-driven Core-collapse Supernova Explosions. *Astrophys J* 799:5, DOI 10.1088/0004-637X/799/1/5, 1408.1399
- Couch SM, Chatzopoulos E, Arnett WD, Timmes FX (2015) The Three-dimensional Evolution to Core Collapse of a Massive Star. *Astrophys J Lett* 808:L21, DOI 10.1088/2041-8205/808/1/L21, 1503.02199
- Ertl T, Janka HT, Woosley SE, Sukhbold T, Ugliano M (2016) A Two-parameter Criterion for Classifying the Explodability of Massive Stars by the Neutrino-driven Mechanism. *Astrophys J* 818:124, DOI 10.3847/0004-637X/818/2/124, 1503.07522
- Fernández R (2012) Hydrodynamics of Core-collapse Supernovae at the Transition to Explosion. I. Spherical Symmetry. *Astrophys J* 749:142, DOI 10.1088/0004-637X/749/2/142, 1111.0665
- Fernández R (2015) Three-dimensional simulations of SASI- and convection-dominated core-collapse supernovae. *Monthly Notices R Astron Soc* 452:2071–2086, DOI 10.1093/mnras/stv1463, 1504.07996
- Fernández R, Müller B, Foglizzo T, Janka HT (2014) Characterizing SASI- and convection-dominated core-collapse supernova explosions in two dimensions. *Monthly Notices R Astron Soc* 440:2763–2780, DOI 10.1093/mnras/stu408, 1310.0469
- Fischer T, Whitehouse SC, Mezzacappa A, Thielemann FK, Liebendörfer M (2010) Protoneutron star evolution and the neutrino-driven wind in general relativistic neutrino radiation hydrodynamics simulations. *Astron Astrophys* 517:A80, DOI 10.1051/0004-6361/200913106, 0908.1871
- Foglizzo T, Scheck L, Janka HT (2006) Neutrino-driven Convection versus Advection in Core-Collapse Supernovae. *Astrophys J* 652:1436–1450, DOI 10.1086/508443, arXiv:astro-ph/0507636
- Foglizzo T, Galletti P, Scheck L, Janka HT (2007) Instability of a Stalled Accretion Shock: Evidence for the Advective-Acoustic Cycle. *Astrophys J* 654:1006–1021, DOI 10.1086/509612
- Foglizzo T, Kazeroni R, Guilet J, Masset F, González M, Krueger BK, Novak J, Oertel M, Margueron J, Faure J, Martin N, Blottiau P, Peres B, Durand G (2015) The Explosion Mechanism of Core-Collapse Supernovae: Progress in Supernova Theory and Experiments. *Publications of the Astron Soc of Australia* 32:e009, DOI 10.1017/pasa.2015.9, 1501.01334
- Grefenstette BW, Harrison FA, Boggs SE, Reynolds SP, Fryer CL, Madsen KK, Wik DR, Zoglauer A, Ellinger CI, Alexander DM, An H, Barret D, Christensen FE, Craig WW, Forster K, Giommi P, Hailey CJ, Hornstrup A, Kaspi VM, Kitaguchi T, Koglin JE, Mao PH, Miyasaka H, Mori K, Perri M, Pivovarov MJ, Puccetti S, Rana V, Stern D, Westergaard NJ, Zhang WW (2014) Asymmetries in core-collapse supernovae from maps of radioactive ^{44}Ti in Cassiopeia A. *Nature* 506:339–342, DOI 10.1038/nature12997, 1403.4978
- Guilet J, Sato J, Foglizzo T (2010) The Saturation of SASI by Parasitic Instabilities. *Astrophys J* 713:1350–1362, DOI 10.1088/0004-637X/713/2/1350, 0910.3953
- Hammer NJ, Janka HT, Müller E (2010) Three-dimensional Simulations of Mixing Instabilities in Supernova Explosions. *Astrophys J* 714:1371–1385, DOI 10.1088/0004-637X/714/2/1371, 0908.3474
- Hanke F, Marek A, Müller B, Janka HT (2012) Is Strong SASI Activity the Key to Successful Neutrino-driven Supernova Explosions? *Astrophys J* 755:138, DOI 10.1088/0004-637X/755/2/138, 1108.4355

- Heger A, Woosley SE (2010) Nucleosynthesis and Evolution of Massive Metal-free Stars. *Astrophys J* 724:341–373, DOI 10.1088/0004-637X/724/1/341, 0803.3161
- Heger A, Woosley SE, Spruit HC (2005) Presupernova Evolution of Differentially Rotating Massive Stars Including Magnetic Fields. *Astrophys J* 626:350–363, DOI 10.1086/429868, arXiv:astro-ph/0409422
- Herant M, Benz W, Hix WR, Fryer CL, Colgate SA (1994) Inside the supernova: A powerful convective engine. *Astrophys J* 435:339–361, DOI 10.1086/174817
- Hirata K, Kajita T, Koshiba M, Nakahata M, Oyama Y (1987) Observation of a neutrino burst from the supernova SN1987A. *Physical Review Letters* 58:1490–1493, DOI 10.1103/PhysRevLett.58.1490
- Hix WR, Messer OE, Mezzacappa A, Liebendörfer M, Sampaio J, Langanke K, Dean DJ, Martínez-Pinedo G (2003) Consequences of Nuclear Electron Capture in Core Collapse Supernovae. *Physical Review Letters* 91(20):201102, DOI 10.1103/PhysRevLett.91.201102, astro-ph/0310883
- Hobbs G, Lorimer DR, Lyne AG, Kramer M (2005) A statistical study of 233 pulsar proper motions. *Monthly Notices R Astron Soc* 360:974–992, DOI 10.1111/j.1365-2966.2005.09087.x, astro-ph/0504584
- Janka HT (2001) Conditions for shock revival by neutrino heating in core-collapse supernovae. *Astron Astrophys* 368:527–560, DOI 10.1051/0004-6361:20010012
- Janka HT (2012) Explosion Mechanisms of Core-Collapse Supernovae. *Annual Review of Nuclear and Particle Science* 62:407–451, DOI 10.1146/annurev-nucl-102711-094901, 1206.2503
- Janka HT (2016) Neutron star kicks by the gravitational tug-boat mechanism in asymmetric supernova explosions: progenitor and explosion dependence. *Astrophys J*, submitted, 1611.07562
- Janka HT, Keil W (1998) Perspectives of Core-Collapse Supernovae beyond SN 1987A. In: L Labhardt, B Binggeli, & R Buser (ed) *Supernovae and cosmology*. Astronomisches Institut der Universität Basel, Basel, p 7, arXiv:astro-ph/9709012
- Janka HT, Müller E (1994) Neutron star recoils from anisotropic supernovae. *Astron Astrophys* 290:496–502
- Janka HT, Müller E (1995) The First Second of a Type II Supernova: Convection, Accretion, and Shock Propagation. *Astrophys J Lett* 448:L109–L113, DOI 10.1086/309604
- Janka HT, Müller E (1996) Neutrino heating, convection, and the mechanism of Type-II supernova explosions. *Astron Astrophys* 306:167–198
- Janka HT, Kifonidis K, Rampp M (2001) Supernova Explosions and Neutron Star Formation. In: D Blaschke, N K Glendenning, & A Sedrakian (ed) *Physics of Neutron Star Interiors*, Lecture Notes in Physics, Berlin Springer Verlag, vol 578, p 333
- Janka HT, Langanke K, Marek A, Martínez-Pinedo G, Müller B (2007a) Theory of core-collapse supernovae. *Physics Reports* 442:38–74, DOI 10.1016/j.physrep.2007.02.002, astro-ph/0612072
- Janka HT, Langanke K, Marek A, Martínez-Pinedo G, Müller B (2007b) Theory of core-collapse supernovae. *Physics Reports* 442:38–74, DOI 10.1016/j.physrep.2007.02.002, astro-ph/0612072
- Janka HT, Müller B, Kitaura FS, Buras R (2008) Dynamics of shock propagation and nucleosynthesis conditions in O-Ne-Mg core supernovae. *Astron Astrophysics* 485:199–208, DOI 10.1051/0004-6361:20079334
- Janka HT, Hanke F, Hüdepohl L, Marek A, Müller B, Obergaulinger M (2012) Core-collapse supernovae: Reflections and directions. *Progress of Theoretical and Experimental Physics* 2012(1):01A309, DOI 10.1093/ptep/pts067, 1211.1378
- Janka HT, Melson T, Summa A (2016) Physics of Core-Collapse Supernovae in Three Dimensions: A Sneak Preview. *Annual Review of Nuclear and Particle Science* 66:341–375, DOI 10.1146/annurev-nucl-102115-044747, 1602.05576
- Kifonidis K, Plewa T, Janka HT, Müller E (2003) Non-spherical core collapse supernovae. I. Neutrino-driven convection, Rayleigh-Taylor instabilities, and the formation and propagation of metal clumps. *Astron Astrophys* 408:621–649, DOI 10.1051/0004-6361:20030863, arXiv:astro-ph/0302239

- Kifonidis K, Plewa T, Scheck L, Janka HT, Müller E (2006) Non-spherical core collapse supernovae. II. The late-time evolution of globally anisotropic neutrino-driven explosions and their implications for SN 1987 A. *Astron Astrophys* 453:661–678, DOI 10.1051/0004-6361:20054512, arXiv:astro-ph/0511369
- Kitaura FS, Janka HT, Hillebrandt W (2006) Explosions of O-Ne-Mg cores, the Crab supernova, and subluminescent type II-P supernovae. *Astron Astrophys* 450:345–350, DOI 10.1051/0004-6361:20054703
- Kuroda T, Kotake K, Takiwaki T (2016) A New Gravitational-wave Signature from Standing Accretion Shock Instability in Supernovae. *Astrophys J Lett* 829:L14, DOI 10.3847/2041-8205/829/1/L14, 1605.09215
- Lai D, Chernoff DF, Cordes JM (2001) Pulsar Jets: Implications for Neutron Star Kicks and Initial Spins. *Astrophys J* 549:1111–1118, DOI 10.1086/319455, astro-ph/0007272
- Langanke K, Martínez-Pinedo G, Sampaio JM, Dean DJ, Hix WR, Messer OE, Mezzacappa A, Liebendörfer M, Janka HT, Rampp M (2003) Electron Capture Rates on Nuclei and Implications for Stellar Core Collapse. *Physical Review Letters* 90(24):241102, DOI 10.1103/PhysRevLett.90.241102, astro-ph/0302459
- Lentz EJ, Bruenn SW, Hix WR, Mezzacappa A, Messer OEB, Endeve E, Blondin JM, Harris JA, Marronetti P, Yakunin KN (2015) Three-dimensional Core-collapse Supernova Simulated Using a $15 M_{\odot}$ Progenitor. *Astrophys J Lett* 807:L31, DOI 10.1088/2041-8205/807/2/L31, 1505.05110
- Marek A, Janka HT (2009) Delayed Neutrino-Driven Supernova Explosions Aided by the Standing Accretion-Shock Instability. *Astrophys J* 694:664–696, DOI 10.1088/0004-637X/694/1/664, 0708.3372
- Melson T, Janka HT, Bollig R, Hanke F, Marek A, Müller B (2015a) Neutrino-driven Explosion of a 20 Solar-mass Star in Three Dimensions Enabled by Strange-quark Contributions to Neutrino-Nucleon Scattering. *Astrophys J Lett* 808:L42, DOI 10.1088/2041-8205/808/2/L42, 1504.07631
- Melson T, Janka HT, Marek A (2015b) Neutrino-driven Supernova of a Low-mass Iron-core Progenitor Boosted by Three-dimensional Turbulent Convection. *Astrophys J Lett* 801:L24, DOI 10.1088/2041-8205/801/2/L24, 1501.01961
- Müller B (2015) The dynamics of neutrino-driven supernova explosions after shock revival in 2D and 3D. *Monthly Notices R Astron Soc* 453:287–310, DOI 10.1093/mnras/stv1611, 1506.05139
- Müller B (2016) The Status of Multi-Dimensional Core-Collapse Supernova Models. *Publications of the Astron Soc of Australia* 33:e048, DOI 10.1017/pasa.2016.40, 1608.03274
- Müller B, Janka HT (2014) A New Multi-dimensional General Relativistic Neutrino Hydrodynamics Code for Core-collapse Supernovae. IV. The Neutrino Signal. *Astrophys J* 788:82, DOI 10.1088/0004-637X/788/1/82, 1402.3415
- Müller B, Janka HT (2015) Non-radial instabilities and progenitor asphericities in core-collapse supernovae. *Monthly Notices R Astron Soc* 448:2141–2174, DOI 10.1093/mnras/stv101, 1409.4783
- Müller B, Heger A, Liptai D, Cameron JB (2016a) A simple approach to the supernova progenitor-explosion connection. *Monthly Notices R Astron Soc* 460:742–764, DOI 10.1093/mnras/stw1083, 1602.05956
- Müller B, Viallet M, Heger A, Janka HT (2016b) The Last Minutes of Oxygen Shell Burning in a Massive Star. *Astrophys J* 833:124, DOI 10.3847/1538-4357/833/1/124, 1605.01393
- Murphy JW, Burrows A (2008) Criteria for Core-Collapse Supernova Explosions by the Neutrino Mechanism. *Astrophys J* 688:1159–1175, DOI 10.1086/592214, 0805.3345
- Murphy JW, Meakin C (2011) A Global Turbulence Model for Neutrino-driven Convection in Core-collapse Supernovae. *Astrophys J* 742:74, DOI 10.1088/0004-637X/742/2/74, 1106.5496
- Murphy JW, Dolence JC, Burrows A (2013) The Dominance of Neutrino-driven Convection in Core-collapse Supernovae. *Astrophys J* 771:52, DOI 10.1088/0004-637X/771/1/52, 1205.3491

- Nakamura K, Takiwaki T, Kuroda T, Kotake K (2015) Systematic features of axisymmetric neutrino-driven core-collapse supernova models in multiple progenitors. *Publications of the Astron Soc of Australia* 67:107, DOI 10.1093/pasj/psv073, 1406.2415
- Nomoto K (1984) Evolution of 8–10 solar mass stars toward electron capture supernovae. I – Formation of electron-degenerate O+Ne+Mg cores. *Astrophys J* 277:791–805, DOI 10.1086/161749
- Nomoto K (1987) Evolution of 8–10 solar mass stars toward electron capture supernovae. II – Collapse of an O+Ne+Mg core. *Astrophys J* 322:206–214, DOI 10.1086/165716
- Nomoto K, Hashimoto M (1988) Presupernova evolution of massive stars. *Physics Reports* 163:13–36, DOI 10.1016/0370-1573(88)90032-4
- Nomoto K, Sugimoto D, Sparks WM, Fesen RA, Gull TR, Miyaji S (1982) The Crab Nebula's progenitor. *Nature* 299:803–805, DOI 10.1038/299803a0
- Nordhaus J, Burrows A, Almgren A, Bell J (2010) Dimension as a Key to the Neutrino Mechanism of Core-collapse Supernova Explosions. *Astrophys J* 720:694–703, DOI 10.1088/0004-637X/720/1/694, 1006.3792
- O'Connor E, Ott CD (2011) Black Hole Formation in Failing Core-Collapse Supernovae. *Astrophys J* 730:70, DOI 10.1088/0004-637X/730/2/70, 1010.5550
- Owen PJ, Barlow MJ (2015) The Dust and Gas Content of the Crab Nebula. *Astrophys J* 801:141, DOI 10.1088/0004-637X/801/2/141, 1501.01510
- Pejcha O, Thompson TA (2012) The Physics of the Neutrino Mechanism of Core-collapse Supernovae. *Astrophys J* 746:106, DOI 10.1088/0004-637X/746/1/106, 1103.4864
- Pejcha O, Thompson TA (2015) The Landscape of the Neutrino Mechanism of Core-collapse Supernovae: Neutron Star and Black Hole Mass Functions, Explosion Energies, and Nickel Yields. *Astrophys J* 801:90, DOI 10.1088/0004-637X/801/2/90, 1409.0540
- Qian YZ, Woosley SE (1996) Nucleosynthesis in Neutrino-driven Winds. I. The Physical Conditions. *Astrophys J* 471:331, DOI 10.1086/177973, arXiv:astro-ph/9611094
- Radice D, Couch SM, Ott CD (2015) Implicit large eddy simulations of anisotropic weakly compressible turbulence with application to core-collapse supernovae. *Computational Astrophysics and Cosmology* 2:7, DOI 10.1186/s40668-015-0011-0, 1501.03169
- Radice D, Ott CD, Abdikamalov E, Couch SM, Haas R, Schnetter E (2016) Neutrino-driven Convection in Core-collapse Supernovae: High-resolution Simulations. *Astrophys J* 820:76, DOI 10.3847/0004-637X/820/1/76, 1510.05022
- Roberts LF, Ott CD, Haas R, O'Connor EP, Diener P, Schnetter E (2016) General-Relativistic Three-Dimensional Multi-group Neutrino Radiation-Hydrodynamics Simulations of Core-Collapse Supernovae. *Astrophys J* 831:98, DOI 10.3847/0004-637X/831/1/98, 1604.07848
- Scheck L, Kifonidis K, Janka HT, Müller E (2006) Multidimensional supernova simulations with approximative neutrino transport. I. Neutron star kicks and the anisotropy of neutrino-driven explosions in two spatial dimensions. *Astron Astrophys* 457:963–986, DOI 10.1051/0004-6361:20064855, arXiv:astro-ph/0601302
- Scheck L, Janka HT, Foglizzo T, Kifonidis K (2008) Multidimensional supernova simulations with approximative neutrino transport. II. Convection and the advective-acoustic cycle in the supernova core. *Astron Astrophys* 477:931–952, DOI 10.1051/0004-6361:20077701, 0704.3001
- Shapiro SL, Teukolsky SA (1983) *Black holes, white dwarfs, and neutron stars: The physics of compact objects*. Wiley, New York
- Smartt SJ (2015) Observational Constraints on the Progenitors of Core-Collapse Supernovae: The Case for Missing High-Mass Stars. *Publications of the Astron Soc of Australia* 32:e016, DOI 10.1017/pasa.2015.17, 1504.02635
- Sukhbold T, Woosley SE (2014) The Compactness of Presupernova Stellar Cores. *Astrophys J* 783:10, DOI 10.1088/0004-637X/783/1/10, 1311.6546
- Sukhbold T, Ertl T, Woosley SE, Brown JM, Janka HT (2016) Core-collapse Supernovae from 9 to 120 Solar Masses Based on Neutrino-powered Explosions. *Astrophys J* 821:38, DOI 10.3847/0004-637X/821/1/38, 1510.04643

- Summa A, Hanke F, Janka HT, Melson T, Marek A, Müller B (2016) Progenitor-dependent Explosion Dynamics in Self-consistent, Axisymmetric Simulations of Neutrino-driven Core-collapse Supernovae. *Astrophys J* 825:6, DOI 10.3847/0004-637X/825/1/6, 1511.07871
- Takiwaki T, Kotake K, Suwa Y (2012) Three-dimensional Hydrodynamic Core-collapse Supernova Simulations for an 11.2 M_{\odot} Star with Spectral Neutrino Transport. *Astrophys J* 749:98, DOI 10.1088/0004-637X/749/2/98, 1108.3989
- Takiwaki T, Kotake K, Suwa Y (2014) A Comparison of Two- and Three-dimensional Neutrino-hydrodynamics Simulations of Core-collapse Supernovae. *Astrophys J* 786:83, DOI 10.1088/0004-637X/786/2/83, 1308.5755
- Tamborra I, Hanke F, Müller B, Janka HT, Raffelt G (2013) Neutrino Signature of Supernova Hydrodynamical Instabilities in Three Dimensions. *Physical Review Letters* 111(12):121104, DOI 10.1103/PhysRevLett.111.121104, 1307.7936
- Tamborra I, Hanke F, Janka HT, Müller B, Raffelt GG, Marek A (2014a) Self-sustained Asymmetry of Lepton-number Emission: A New Phenomenon during the Supernova Shock-accretion Phase in Three Dimensions. *Astrophys J* 792:96, DOI 10.1088/0004-637X/792/2/96, 1402.5418
- Tamborra I, Raffelt G, Hanke F, Janka HT, Müller B (2014b) Neutrino emission characteristics and detection opportunities based on three-dimensional supernova simulations. *Phys Rev D* 90(4):045032, DOI 10.1103/PhysRevD.90.045032, 1406.0006
- Thompson TA, Burrows A, Meyer BS (2001) The Physics of Proto-Neutron Star Winds: Implications for r-Process Nucleosynthesis. *Astrophys J* 562:887–908, DOI 10.1086/323861, arXiv:astro-ph/0105004
- Thompson TA, Quataert E, Burrows A (2005) Viscosity and Rotation in Core-Collapse Supernovae. *Astrophys J* 620:861–877, DOI 10.1086/427177
- Ugliano M, Janka HT, Marek A, Arcones A (2012) Progenitor-explosion Connection and Remnant Birth Masses for Neutrino-driven Supernovae of Iron-core Progenitors. *Astrophys J* 757:69, DOI 10.1088/0004-637X/757/1/69, 1205.3657
- Utrobin VP, Wongwathanarat A, Janka HT, Müller E (2015) Supernova 1987A: neutrino-driven explosions in three dimensions and light curves. *Astron Astrophys* 581:A40, DOI 10.1051/0004-6361/201425513, 1412.4122
- Wanajo S, Janka HT, Müller B (2011) Electron-capture Supernovae as The Origin of Elements Beyond Iron. *Astrophys J Lett* 726:L15, DOI 10.1088/2041-8205/726/2/L15, 1009.1000
- Wanajo S, Janka HT, Müller B (2013a) Electron-capture Supernovae as Origin of ^{48}Ca . *Astrophys J Lett* 767:L26, DOI 10.1088/2041-8205/767/2/L26, 1302.0929
- Wanajo S, Janka HT, Müller B (2013b) Electron-capture Supernovae as Sources of ^{60}Fe . *Astrophys J Lett* 774:L6, DOI 10.1088/2041-8205/774/1/L6, 1307.3319
- Wilson JR (1985) Supernovae and Post-Collapse Behavior. In: Centrella JM, Leblanc JM, Bowers RL (eds) *Numerical Astrophysics*. Jones and Bartlett Publishers, Boston, pp 422–434
- Wongwathanarat A, Janka H, Müller E (2010) Hydrodynamical Neutron Star Kicks in Three Dimensions. *Astrophys J Lett* 725:L106–L110, DOI 10.1088/2041-8205/725/1/L106, 1010.0167
- Wongwathanarat A, Janka HT, Müller E (2013) Three-dimensional neutrino-driven supernovae: Neutron star kicks, spins, and asymmetric ejection of nucleosynthesis products. *Astron Astrophys* 552:A126, DOI 10.1051/0004-6361/201220636, 1210.8148
- Wongwathanarat A, Müller E, Janka HT (2015) Three-dimensional simulations of core-collapse supernovae: from shock revival to shock breakout. *Astron Astrophys* 577:A48, DOI 10.1051/0004-6361/201425025, 1409.5431
- Wongwathanarat A, Janka HT, Mueller E, Pllumbi E, Wanajo S (2016) Production and Distribution of ^{44}Ti and ^{56}Ni in a Three-dimensional Supernova Model Resembling Cassiopeia A. *Astrophys J*, submitted, 1610.05643
- Woolsey SE, Heger A (2015a) Erratum: “Long Gamma-Ray Transients from Collapsars” (2012, *ApJ*, 752, 32). *Astrophys J* 806:145, DOI 10.1088/0004-637X/806/1/145
- Woolsey SE, Heger A (2015b) The Remarkable Deaths of 9–11 Solar Mass Stars. *Astrophys J* 810:34, DOI 10.1088/0004-637X/810/1/34, 1505.06712

- Woosley SE, Heger A, Weaver TA (2002) The evolution and explosion of massive stars. *Reviews of Modern Physics* 74:1015–1071, DOI 10.1103/RevModPhys.74.1015
- Yamasaki T, Yamada S (2006) Standing Accretion Shocks in the Supernova Core: Effects of Convection and Realistic Equations of State. *Astrophys J* 650:291–298, DOI 10.1086/507067, arXiv:astro-ph/0606504
- Yang H, Chevalier RA (2015) Evolution of the Crab Nebula in a Low Energy Supernova. *Astrophys J* 806:153, DOI 10.1088/0004-637X/806/2/153, 1505.03211